

Research Paper

Near-infrared light-regulated cancer theranostic nanoplatform based on aggregation-induced emission luminogen encapsulated upconversion nanoparticles

Guorui Jin^{1,2*}, Rongyan He^{1,2*}, Qian Liu^{1,2}, Min Lin^{1,2}, Yuqing Dong^{2,3}, Kai Li⁴, Ben Zhong Tang^{5,6}, Bin Liu⁷✉, Feng Xu^{1,2}✉

1. The Key Laboratory of Biomedical Information Engineering of Ministry of Education, School of Life Science and Technology, Xi'an Jiaotong University, Shaanxi, 710049, China
2. Bioinspired Engineering & Biomechanics Center (BEBC), Xi'an Jiaotong University, Shaanxi, 710049, China
3. State Key Laboratory for Mechanical Behavior of Materials, School of Materials Science and Engineering, Xi'an Jiaotong University, Xi'an 710049, People's Republic of China
4. Department of Biomedical Engineering, Southern University of Science and Technology, Shenzhen, Guangdong 510855, China.
5. Department of Chemistry, Institute for Advanced Study, Institute of Molecular Functional Materials, Division of Biomedical Engineering, Division of Life Science, and State Key Laboratory of Molecular Neuroscience, The Hong Kong University of Science & Technology, Clear Water Bay, Kowloon, Hong Kong, China
6. Guangdong Innovative Research Team, SCUT-HKUST Joint Research Laboratory, State Key Laboratory of Luminescent Materials and Devices, South China University of Technology, Guangzhou, 510640, China
7. Department of Chemical and Biomolecular Engineering, National University of Singapore, 4 Engineering Drive 4, 117585, Singapore.

*Authors contributed equally

✉ Corresponding author: cheliub@nus.edu.sg; fengxu@mail.xjtu.edu.cn

© Ivyspring International Publisher. This is an open access article distributed under the terms of the Creative Commons Attribution (CC BY-NC) license (<https://creativecommons.org/licenses/by-nc/4.0/>). See <http://ivyspring.com/terms> for full terms and conditions.

Received: 2018.09.25; Accepted: 2018.11.13; Published: 2019.01.01

Abstract

Photodynamic therapy (PDT) has been widely applied in the clinic for the treatment of various types of cancer due to its precise controllability, minimally invasive approach and high spatiotemporal accuracy as compared with conventional chemotherapy. However, the porphyrin-based photosensitizers (PSs) used in clinics generally suffer from aggregation-caused reductions in the generation of reactive oxygen species (ROS) and limited tissue penetration because of visible light activation, which greatly hampers their applications for the treatment of deep-seated tumors.

Methods: We present a facile strategy for constructing a NIR-regulated cancer theranostic nanoplatform by encapsulating upconversion nanoparticles (UCNPs) and a luminogen (2-(2,6-bis((E)-4-(phenyl(40-(1,2,2-triphenylvinyl)-[1,10-biphenyl]-4-yl)amino)styryl)-4H-pyran-4-ylidene)malononitrile, TTD) with aggregation-induced emission (AIEgen) characteristics using an amphiphilic polymer, and further conjugating cyclic arginine-glycine-aspartic acid (cRGD) peptide to yield UCNP@TTD-cRGD NPs. We then evaluated the bioimaging and anti-tumor capability of the UCNP@TTD-cRGD NPs under NIR light illumination in an *in vitro* three-dimensional (3D) cancer spheroid and in a murine tumor model, respectively.

Results: With a close match between the UCNP emission and absorption of the AIEgen, the synthesized NPs could efficiently generate ROS, even under excitation through thick tissues. The NIR-regulated UCNP@TTD-cRGD NPs that were developed could selectively light up the targeted cancer cells and significantly inhibit tumor growth during the NIR-regulated PDT treatment as compared with the cells under white light excitation.

Conclusion: In summary, the synthesized UCNP@TTD-cRGD NPs showed great potential in NIR light-regulated photodynamic therapy of deep-seated tumors. Our study will inspire further exploration of novel theranostic nanoplatforms that combine UCNPs and various AIEgen PSs for the advancement of deep-seated tumor treatments with potential clinical translations.

Key words: aggregation-induced emission (AIE), photodynamic therapy, near infrared light, active targeting, tumor imaging

Introduction

While numerous advances have been made in cancer diagnosis and chemotherapy, cancer patients still suffer from severe side effects, drug resistance and frequent recurrence of cancer [1]. This serves to emphasize the importance of developing new antitumor therapy strategies that have new mechanisms of action. Nanoparticle-based theranostic platforms that incorporate both imaging and therapeutic reagents into one single probe are strongly desired for cancer diagnosis and treatment because they facilitate image-guided diagnosis and therapy concurrently [2-4]. Among the various theranostic platforms, photodynamic therapy (PDT) has been increasingly recognized as an attractive approach for cancer treatment because of the advantages of precise controllability, its minimally invasive nature and high spatiotemporal accuracy [5-11]. PDT relies on photosensitizers (PSs) to generate toxic reactive oxygen species (ROS) to induce cell death upon light illumination, while the fluorescence from the photosensitizers can also facilitate the image-guided theranostic process. However, traditional fluorescent photosensitizers, especially the clinically used porphyrin derivatives, generally suffer from π - π stacking due to the intrinsic hydrophobic and rigid planar molecular structures, which further lead to aggregation caused quenching (ACQ) and a significant decrease in ROS generation [12, 13]. Additionally, the requirement of visible light activation for most of the conventional PSs greatly hampers their clinical applications in treating solid or deep-seated tumors, due to the limited tissue-penetration depth of visible light [14]. Therefore, there is an unmet demand for developing effective PDT PSs with good ROS yield and stable fluorescence in an aggregated state, which can be activated by near-infrared (NIR) light that has greater tissue-penetration depth and less tissue scattering and blood absorption [15, 16].

Fluorogens with aggregation-induced emission characteristics (AIEgens) have emerged as effective fluorescent materials for theranostic applications [17-19]. In contrast to ACQ materials, AIEgens are generally non-emissive in good solutions but can become highly emissive upon aggregation, due to the restriction of intramolecular rotations, which prohibits energy dissipation through nonradiative channels [20]. As such, AIEgen PSs have attracted significantly increasing interest as excellent key components in PDTs with the expectation of yielding bright emission and high ROS-induced phototoxicity upon loading into nanocarriers in an aggregated state [21-23]. Additionally, by taking advantage of the AIE phenomenon, AIEgens have been developed further

as activatable PSs via triggered aggregation to further optimize the therapeutic outcome of PDTs and to increase the signal-to-background ratio in bioimaging [24-27]. However, most AIEgen PSs are regulated by visible light (400–700 nm) which suffers from limited tissue-penetration depth, thus restricting their applications to only therapy for superficial cancers (*e.g.*, melanoma) [28, 29]. Recently, AIEgen PSs with two-photon absorption (TPA) capability have been developed to realize NIR light-regulated PDTs using expensive femtosecond pulsed lasers [29]. However, this requires complicated synthesis routines which are not feasible for obtaining AIEgen PSs with usable TPA efficiency [30]. In addition, two-photon-PDT treatment is restricted to a tiny tissue volume resulting in prolonged treatment time, thus limiting its clinical use [31]. Therefore, there is still an unmet need for a facile and efficient approach to solve these issues to further extend the applications of AIEgen PSs across a broad range of cancer therapies.

Upconversion nanoparticles (UCNPs), which can harness energy from NIR light and convert it to higher energy (*e.g.*, visible or UV light) [32, 33], have emerged as a promising NIR light “transducer” to engineer NIR light-regulated theranostic nanoplatforams for PDTs to solve the issue of limited tissue-penetration depth [34-36]. Therefore, by choosing UCNPs whose emission spectra match the absorption spectrum of AIEgen PSs, a robust NIR light-regulated theranostic platform can be engineered for the treatment of deep-seated tumors. This facile and efficient strategy thus greatly expands the potential applications of AIEgen PSs in treating a broad range of cancers. To the best of our knowledge, the *in vivo* PDT of deep-seated tumors based on the combination of UCNPs with an AIEgen PS has not been reported yet.

In this research work, we developed a monodisperse nanoplatforam by direct encapsulation of UCNPs with a spectrally matchable AIEgen PS, which offers targeted cell imaging and PDT under single NIR laser illumination. By encapsulating the hydrophobic AIEgen, 2-(2,6-bis((E)-4-(phenyl(40-(1,2,2-triphenylvinyl)-[1,10-biphenyl]-4-yl)amino)styryl)-4H-pyran-4-ylidene)malononitrile (TTD) and UCNPs using a biocompatible poly(ethylene glycol)-lipid and further decoration of the particle surface with cyclic arginine-glycine-aspartic acid (cRGD), we obtained NIR-regulated multifunctional probes (*i.e.*, UCNP@TTD-cRGD) for the PDT treatment of cancer. The synthesized UCNP@TTD-cRGD can still efficiently generate ROS in the presence of a 6 mm thick tissue when excited by a 980 nm laser. In addition, the UCNP@TTD-cRGD could selectively and efficiently kill the targeted triple

negative breast cancer cells (MDA-MB-231) as demonstrated in both two-dimensional (2D) and three-dimensional (3D) *in vitro* tumor models. The therapeutic efficacy of UCNP@TTD-cRGD NPs as an *in vivo* PDT agent was further evaluated in a mouse model. After 980 nm laser illumination, the growth of tumors intratumorally injected with the NPs was significantly inhibited despite the different initial sizes (60, 120 and 240 mm³), indicating an excellent PDT efficacy of the UCNP@TTD-cRGD NPs in deep-seated tumor treatments. Additionally, the UCNP@TTD-cRGD NPs could accumulate at the tumor site for tumor imaging and significant restriction of tumor growth after intravenous administration. These results demonstrate that the NIR light-regulated cancer theranostic nanoplatform with AIEgen PSs will open up new opportunities for targeted and image-guided PDT of deep-seated tumors allowing for great clinical translation potential.

Materials and methods

Synthesis of upconversion nanoparticles (UCNPs)

The NaYF₄:Yb,Er UCNPs were synthesized according to reports in the literature [2, 37]. Briefly, deionized water (2 mL) containing YCl₃·6H₂O (242.69 mg, 0.8 mmol), YbCl₃·6H₂O (69.75 mg, 0.18 mmol), and ErCl₃·6H₂O (7.64 mg, 0.02 mmol) was added to a 100 mL flask that was pre-loaded with oleic acid (7.5 mL) and 1-octadecene (15 mL). The solution was stirred for 0.5 h at room temperature, followed by stirring for 1 h at 120 °C, and for another 1.5 h at 166 °C to remove water under an argon atmosphere. After the solution was cooled down to room temperature, a methanol solution (5 mL) with NH₄F (148.15 mg, 4 mmol) and NaOH (100 mg, 2.5 mmol) was added, and it was further stirred for 2 h. Then, the methanol was removed by heating the solution to 120 °C for 1 h. The solution was further heated to 296 °C for 2 h, followed by a cooling down to room temperature. The resulting product was washed with ethanol and cyclohexane three times and then finally dissolved in tetrahydrofuran (THF).

Synthesis of UCNP@TTD-cRGD NPs

To synthesize UCNP@TTD-cRGD NPs, 2 mL THF was used to dissolve DSPE-PEG₂₀₀₀-Mal (2 mg), DSPE-PEG₂₀₀₀ (1 mg) and TTD molecules (0.75 mg). The UCNPs dissolved in THF (70 µL, 0.4 mg/mL) were added into the formed solution and mixed under sonication for 5 min followed by standing for 30 min. Then the formed mixture solution was quickly injected into 18 mL of deionized (DI) water, and

sonicated immediately for 1.5 min using a probe sonicator at 60 W output to form UCNP@TTD NPs. The THF was evaporated by stirring the clear red solution in the fume hood for 8 h. The cRGD peptides (5×10⁻² M) were then added to the solution containing UCNP@TTD NPs with further stirring at room temperature for 12 h. Then we removed the excess cRGD peptides from the particle solution by dialysis against MilliQ water for 1.5 d and changed it with fresh MilliQ water four times. The UCNP@TTD-cRGD NPs that were generated were collected for further use.

Characterizations

To verify the aggregation-induced luminescence phenomenon, the same amount of molecular AIEgens were dissolved in THF and a water mixture solution with different water fractions (fw) at the same total volume (the water fraction was from 0% to 100% with 10% intervals). The change in fluorescence intensity was measured with a fluorometer (Photon Technology International). The average size of the NPs was measured using a Brookhaven Zeta Plus zeta potential analyzer (Brookhaven Instruments, Holtsville, NY). The morphology of the NPs was studied by transmission electron microscopy (Nippon Tekno Co., Ltd). The emission spectra (200–900 nm) of the UCNP@TTD-cRGD NPs and UCNPs were recorded by excitation with a 980 nm laser. To study the photostability of the synthesized NPs, UCNP@TTD-cRGD NPs (25 µg/mL or 5 µg mL⁻¹ of TTD) were dispersed in DMEM supplemented with 10% FBS and 1% PS, and the emission intensity was recorded every day up to 10 days using a fluorometer (Photon Technology International). A Qtracker® 585 (a commercial fluorescent probe) with the same concentration was used as a control.

Detection of ROS in solution

The 9,10-anthracenediyl-bis(methylene) dimalonate (ABDA) probe was sensitive to the singlet oxygen (¹O₂) which was used to measure ¹O₂ generation from the NPs irradiated by a 980 nm laser. The absorbance at 378 nm of ABDA would decrease in the presence of ¹O₂ because of the oxidized ABDA [38]. Rose Bengal (RB) with a 75% ¹O₂ quantum yield in water was used as the standard photosensitizer [39]. The ABDA solid was dissolved in the mixture of UCNP@TTD-cRGD NPs (5 µg mL⁻¹ of TTD) with a concentration of 40 µM and RB (5 µg/mL) and then irradiated for 0, 30, 60, 90 and 120 seconds using a 980 nm laser (for UCNP@TTD-cRGD) and white light (for RB), both at a power density of 200 mW cm⁻². The power output of the white light and 980 nm laser used in this study was measured at 500 nm (the absorbance

maximum of TTD) and at 980 nm using an optical power and energy meter (Thorlabs, PM100D), respectively.

The $^1\text{O}_2$ quantum yield of the UCNP@TTD-cRGD was calculated based on the following equation [39].

$$\Phi_{\text{NPs}} = \Phi_{\text{RB}} \frac{K_{\text{NPs}} I_{\text{RB}}}{K_{\text{RB}} I_{\text{NPs}}}$$

where Φ_{NPs} and Φ_{RB} were the $^1\text{O}_2$ quantum yield for UCNP@TTD-cRGD and RB, respectively. K_{NPs} and K_{RB} represent the slope of plot $\ln(A_0/A)$ versus illumination time from the UCNP@TTD-cRGD and RB, respectively, where A and A_0 stands for the absorbance of ABDA at 378 nm with and without light illumination, respectively. I_{NPs} and I_{RB} were calculated from the areas of their absorption spectra, from 400–800 nm, respectively.

The tissue-penetration ability of UCNP@TTD-cRGD NPs

The UCNP@TTD-cRGD NPs in the cuvettes were covered by chicken tissues of different thicknesses (*i.e.*, 0, 3 and 6 mm), and further illuminated by a 980 nm laser and white light at a power density of 200 mW cm⁻² for 2 min, respectively. Then we used a ROS probe, ABDA to detect the ROS generation.

Targeting capability of UCNP@TTD-cRGD NPs

Coverslips with a diameter of 15 mm were located in a 24-well plate. Three kinds of cells (MDA-MB-231, MCF-7 and NIH 3T3) at a density of 3×10^4 cells per well were seeded on the coverslips, respectively. After 12 h of incubation, the culture medium was replaced by fresh medium supplemented with UCNP@TTD-cRGD NPs (5 $\mu\text{g mL}^{-1}$ of TTD) and the cells were further incubated for 4 h. The cells treated by NPs were fixed by 4% paraformaldehyde for 15 min and washed with 1×PBS buffer twice followed by flow cytometry detection. The NP-treated cells were used for fluorescence imaging study after being stained with 4',6-diamidino-2-phenylindole (DAPI).

Intracellular ROS detection

The CellROX[®] Deep Red Reagent (Thermo Fisher Scientific) was used to detect intracellular ROS, following the manufacturer's instructions. Briefly, The MDA-MB-231 cells treated with UCNP@TTD-cRGD NPs (5 $\mu\text{g mL}^{-1}$ of TTD) were further incubated with CellROX[®] Deep Red Reagent that was diluted to 5 μM with pure DMEM medium for 30 min. Then the cell culture medium was replaced with fresh medium after three times washing with 1×PBS. After that, the cells were subjected to 2 min of 980 nm laser (200 mW

cm⁻²) illumination, followed by fixation with 4% paraformaldehyde. The fixed cells were imaged using confocal microscopy at 644 nm excitation and a 665/20 nm bandpass filter.

Cytotoxicity of the UCNP@TTD-cRGD NPs

The cytotoxicity of the UCNP@TTD-cRGD NPs was studied using a 3-(4,5-dimethyl-2-thiazolyl)-2,5-diphenyl-2-H-tetrazolium bromide (MTT) assay. MDA-MB-231, MCF-7 and NIH 3T3 cells (5×10^3 per well) were co-cultured with UCNP@TTD-cRGD NPs at a concentration of 0, 12.5, 25 and 50 $\mu\text{g/mL}$ in 96-well plates, respectively. After 48 h of incubation, a 100 μL MTT solution (0.5 mg/mL) was added into each well, and incubation continued for a further 3 h. Then, 100 μL DMSO was used to dissolve all the formed precipitates with the help of gentle shaking. The absorbance of MTT at 570 nm was monitored with a microplate reader and the viability of the cells was reflected by comparing the absorbance of the nanoparticle-treated cells to that of the cells incubated with nanoparticle-free medium only.

Photocytotoxicity studies

The photocytotoxicity of UCNP@TTD-cRGD NPs was studied by evaluating the metabolic activity of NP-treated cells after illumination with a 980 nm laser. For this, MDA-MB-231, MCF-7 and NIH 3T3 cells at a density of 5000 cells/well were cultured in 96-well plates, and each type of cells was treated with NPs (25 $\mu\text{g/mL}$) alone, 2 min of 980 nm laser illumination alone, and also 2 min of 980 nm laser illumination with NPs, respectively. After 48 h, cell viability was evaluated by MTT assay. For live/dead staining assay, the cells seeded in 24-well plates at a density of 5×10^4 cells per well were subjected to the same treatments, and then live/dead staining was performed to characterize the viability of cells.

Cell apoptosis assay

The APC Annexin V/Dead Cell Apoptosis Kit (Life Technologies) was used to assess cell apoptosis after the PDT treatment according to the manufacturer's instructions. Briefly, UCNP@TTD-cRGD NP-treated MDA-MB-231 cells (3×10^5 cells/well) in 6-well plates were exposed to a 980 nm laser (200 mW cm⁻²) for 2 min and cultured further for 12, 24 and 48 h, respectively. At each time interval, the cells were collected from the 6-well plate and washed three times with 1× annexin-binding buffer, followed by centrifugation and resuspension in 1× annexin-binding buffer at a concentration of 1×10^6 cells/mL. Then, APC annexin V (5 μL) and SYTOX[®] Green solution (1 μL , 1 μM) were added to each 100 μL cell suspension, respectively. After 15 min

incubation, an additional 1× annexin-binding buffer (400 µL) was added into each sample by gentle mixing and the samples were kept on ice before the flow cytometry test. The stained cells were analyzed by recording the fluorescence emission at 530 nm (excited by 488 nm) and 660 nm (excited by 633 nm). Confocal microscopy was applied to verify the flow cytometry results.

In vitro 3D cell spheroids for PDT treatment

The 3D cell spheroids were fabricated using a microwell approach as reported in our previous study [40]. Briefly, 15% polyethylene glycol-dimethacrylate (PEG-DMA, MW=1000; Polysciences, Inc., Warrington, PA, USA) and 0.5% (v/v) of a photoinitiator (PI), 2-hydroxy-2-methylpropiophenone (TCI, Shanghai Development Co., Ltd., Shanghai, China) were used to fabricate microwells facilitated by a photomask. After UV cross-linking, microwells of 800 µm in diameter and 1 mm in depth were formed. The hydrogel microwell array located in the 24-well plates was sterilized by placing the plate in the biosafety cabinet with ultraviolet light illumination for 4 h. MDA-MB-231 cells at a concentration of 1×10⁶ cells/mL were seeded on the microwells. The cell spheroids were formed after three days' culture. Then the spheroids were fed with UCNP@TTD-cRGD NPs (5 µg mL⁻¹ of TTD) according to the above-mentioned protocol with extended co-culture duration of 12 h. After replacement with fresh medium, the NP-treated spheroids were illuminated under a 980 nm laser (200 mW cm⁻²) for 5, 10, 20 and 30 min, respectively. MTT assay and live/dead staining were used to study the viability of the 3D cell spheroids after 48 h further incubation. The cell spheroids treated with NP-free medium with or without NIR laser illumination were used as the control, respectively. We took three fluorescence images in the Z-direction of each spheroid and analyzed the fluorescence intensity of each with ImageJ software to obtain the ratio of live and dead cells within each spheroid after PDT treatment.

Animal study

All the animal studies conformed to the guidelines set by the Institutional Animal Care Committee of Xi'an Jiaotong University. The tumors were developed by subcutaneously implanting 5×10⁶ MDA-MB-231 cells into the right front flanks of female BALB/c nude mice having an average weight of 20 ± 2 g. Tumor volume was monitored using a caliper and calculated using the following formula: volume = (tumor length) × (tumor width)²/2. When the tumor volume reached 60 mm³, 120 mm³ and 240

mm³, the PDT experiments were then conducted, respectively.

In vivo antitumor efficacy of UCNP@TTD-cRGD NPs with intratumoral injection

For *in vivo* imaging studies, the tumor bearing mice having a tumor size of 120 mm³ were intratumorally injected with 20 µL UCNP@TTD-cRGD NPs (2 mg/mL of TTD). Then, *in vivo* fluorescence images were obtained using an IVIS® Lumina Series III with a 500 nm excitation and a bandpass filter from 550 nm to 750 nm at the designated time intervals (1, 2, and 7 D post-injection). The NP-treated mice were sacrificed after 7 days and the collected organs were immediately imaged *ex vivo* using a IVIS® Lumina Series III with a 500 nm excitation and a bandpass filter from 550 nm to 750 nm.

For *in vivo* PDT treatment using intratumorally injected UCNP@TTD-cRGD NPs, we divided the tumor-bearing mice into three groups based on their initial tumor volumes (60 mm³, 120 mm³ and 240 mm³). Each group included five sub-groups that were treated as follows: control group, without any treatment; nanoparticle-only group, tumors intratumorally injected with nanoparticles only; laser-only group, tumors intratumorally injected with saline with NIR laser illumination (200 mW cm⁻²) for 20 min; white light PDT group, tumors intratumorally injected with UCNP@TTD-cRGD NPs (2 mg/mL, 20 µL), and at 4 h injection illuminated with white light (200 mW cm⁻²) for 20 min; laser PDT group, tumors intratumorally injected with UCNP@TTD-cRGD NPs (2 mg/mL, 20 µL), and a 4 h injection illuminated with a 980 nm laser (200 mW cm⁻²) for 20 min. The tumor volume and mice body weight were measured every two days.

All the mice were euthanized after 10 days' treatment, and the tumors were collected and fixed in 10% neutral-buffered formalin for further evaluation. For the hematoxylin and eosin (H&E) staining, the formalin-fixed tumor sections were stained and visualized by fluorescence microscope (Olympus IX51, Japan). For the TUNEL staining, the fixed tumor sections were stained by the One Step TUNEL Apoptosis Assay Kit (Beyotime Biotechnology, Beijing, China) according to the manufacturer's protocol and visualized by fluorescence microscope (Olympus IX51, Japan).

In vivo targeted PDT treatment with intravenous injection

For investigating the biodistribution of NPs, the tumor bearing mice having a tumor size of 120 mm³ were intravenously injected with 125 µL

UCNP@TTD-cRGD NPs (2 mg/mL of TTD). Then, *in vivo* fluorescence images were obtained using an IVIS® Lumina Series III with a 500 nm excitation light and a bandpass filter from 550 nm to 750 nm at different time intervals (0, 4, 8, 24, 48 and 96 h post-injection). The NP-treated mice were sacrificed after 24 h and the collected organs were immediately imaged *ex vivo* by IVIS® Lumina Series III with a 500 nm excitation and a bandpass filter from 550 nm to 750 nm. Intravenous injection of free cRGD (15 mg kg⁻¹) was conducted to block the overexpressed integrin of the MDA-MB-231 tumors. After injection of free cRGD for 30 min, 125 μL of UCNP@TTD-cRGD NPs (2 mg/mL of TTD) were then intravenously injected into the tumor-bearing mice. The tumor-bearing mice intravenously injected with 125 μL of UCNP@TTD-cRGD NPs (2 mg/mL of TTD) were used as positive control. The mice were then imaged using the IVIS® Lumina Series III following the same protocol.

We chose the tumor-bearing mice with an initial tumor volume of 120 mm³ for further evaluation of the *in vivo* targeted PDT treatment of deep-seated tumors using UCNP@TTD-cRGD NPs administered by intravenous injection. The tumor-bearing mice were randomly divided into five groups: control group, nanoparticle-only group, laser-only group, white light PDT group, and laser PDT group. Both NPs and saline were administered intravenously to tumor-bearing mice in the corresponding groups. The tumor volume and mice body weight were measured every two days.

Hemolysis assay and *in vivo* toxicity assay

Red blood cells (RBCs) were isolated by centrifugation of mice blood at 3000 rpm for 10 min and thrice washed with saline. Then the RBCs were co-cultured with distilled water, saline and the UCNP@TTD-cRGD NP solution (20 μg/mL, 40 μg/mL and 80 μg/mL of TTD), respectively. After culture for the designated time intervals (1, 2 and 3 h), all suspensions were subjected to 5 min centrifugation at 3000 rpm, followed by transfer of the supernatant liquid to a 96-well plate for absorbance reading at 577 nm by a microplate reader (Thermo Scientific, USA). The same concentration of UCNP@TTD-cRGD NPs was suspended in saline as a blank control. The precipitations at the bottom of the tubes were used to make the cell smear to observe the morphologies of the RBCs. The hemolysis ratio of the RBCs was calculated using the following formula:

$$\text{Hemolysis (\%)} = \frac{(\text{OD}_{\text{sample}} - \text{OD}_{\text{negative control}})}{(\text{OD}_{\text{positive control}} - \text{OD}_{\text{blank}})} \times 100\%.$$

Tumor-free mice were used to study the *in vivo*

toxicity of UCNP@TTD-cRGD NPs by collection of the major organs (such as heart, liver, spleen, lung and kidney) from the mice intravenously injected with UCNP@TTD-cRGD NPs after 5 days. Then the organs were fixed, embedded and sectioned for H&E staining. Photos were taken to evaluate the toxicity of the UCNP@TTD-cRGD NPs *in vivo* by comparing the morphology and structure of the major organs with tumor-free mice without nanoparticle injection.

Statistical analysis

All quantitative results were obtained from at least three samples for analysis. Data were expressed as the mean ± standard error of the mean. A two-tailed paired Student's *t*-test was used to compare the differences. Difference with *p* < 0.05 was considered to be statistically significant.

Results and discussion

Preparation of UCNP@TTD-cRGD NPs

In this study, we developed a NIR light-regulated theranostic platform based on AIE-luminogen-encapsulated UCNPs (**Figure 1**). This platform possesses capabilities for enhanced bioimaging and deep-seated tumor treatment, because of the AIEgen PS that can yield bright emission and high ROS-induced phototoxicity in an aggregated state, as well as UCNPs that can convert NIR light to shorter wavelength light for the activation of the AIEgen PS [41, 42]. To achieve high ROS yield, we chose the NaYF₄:Yb,Er UCNPs as the NIR light transducer, as its emission matches well with the excitation of TTD at around 540 nm (**Figure S1**). Briefly, we used amphiphilic polymers (*i.e.*, DSPE-PEG₂₀₀₀ and DSPE-PEG₂₀₀₀-MAL) to encapsulate the hydrophobic UCNPs and TTD that were synthesized according to our previous protocol [43, 44] and synthetic route [17], respectively. The synthesized TTD molecules showed typical twisted intra-molecular charge transfer and AIE characteristics (**Figure 2A**). The DSPE segments along with the hydrophobic UCNPs and TTD tended to be entangled into the hydrophobic core, while the hydrophilic PEG chains spread out into the aqueous phase [45]. The hydrophobic interaction between TTD and the NaYF₄:Yb,Er UCNPs provides a simple method to keep the PS molecule TTD close to the UCNPs, favoring energy transfer between the two components. The formed PEG sheath has the potential to enhance the circulation time of the synthesized NPs, therefore improving nanoparticle accumulation at the tumor site for *in vivo* applications [46]. No obvious precipitation formed in the UCNP@TTD NP suspensions after removing THF, indicating the high encapsulation efficiency of TTD and the UCNPs. The

Mal-decorated UCNP@TTD NPs were further conjugated with cyclic arginine-glycine-aspartic acid (cRGD) peptide to yield UCNP@TTD-cRGD NPs, which have the ability to target integrin-overexpressed cancer cells. The UCNP@TTD-cRGD NPs that were obtained have excellent colloidal stability in a water suspension as demonstrated by the fact that no obvious precipitation was observed even after being stored at 4 °C for 3 months. The bioimaging and anti-tumor capability of UCNP@TTD-cRGD NPs upon NIR light illumination was further evaluated in an *in vitro* three-dimensional (3D) cancer spheroid and in a murine tumor model, respectively.

Characterization of the UCNP@TTD-cRGD NPs

The ideal NP for image-guided PDT applications should have characteristics of monodispersity, photostability, targeting, and a high signal-to-background ratio, as well as negligible dark cytotoxicity and acute cytotoxicity under light illumination [47]. In particular, PS-loaded NPs with excellent monodispersity favor the diffusion of ROS considering the fact that ROS have a small active range (<20 nm) in a PDT protocol [48]. We therefore used dynamic light scattering analysis and transmission electron microscopy to study the dispersity and morphology of the synthesized UCNP@TTD-cRGD NPs. We observed that the monodisperse NPs have a corona morphology and a narrow size distribution of 90 ± 4 nm (Figure 2B and Figure S2). Since a close match between the UCNP emission and absorption of the AIEgen PS is necessary for efficient upconversion to occur, we therefore examined the spectral match between the UCNP emission and absorption of TTD (Figure 2C). We observed that the emission of UCNP upon NIR excitation matches well with the absorption of TTD. As compared with UCNP alone, nearly all the green peaks (~540 nm) of the UCNP were absorbed by the TTD within the UCNP@TTD-cRGD NPs. Moreover, the green color of UCNPs changes to a red color for the UCNP@TTD-cRGD NPs upon 980 nm laser illumination (Figure 2C, insert), further confirming efficient energy transfer between the UCNP and TTD. The enhanced red fluorescence of UCNP@TTD-cRGD NPs favors *in vivo* bioimaging. Since photostability is important for long-term tumor imaging, we checked the photostability of UCNP@TTD-cRGD NPs dispersed in a cell culture medium, using the commercial cell imaging probe Qtracker® 585 as a control (Figure 2D). We observed that UCNP@TTD-cRGD NPs could still maintain 75% of their initial fluorescence after 10 days, while the

fluorescence of Qtracker® 585 was dramatically decreased to ~20% of the initial fluorescence after only 3 days (Figure 2D). The dramatically decreased fluorescence of Qtracker® 585 in a cell culture medium has been reported previously [49, 50]. The probable reason is that the quantum dot-based Qtracker® 585 suffers from potential degradation caused by reactive oxygen species, resulting in a fluorescence decrease [51, 52]. The results indicate that the synthesized UCNP@TTD-cRGD NPs are suitable for long-term imaging applications.

Considering that the generation of cytotoxic singlet oxygen ($^1\text{O}_2$) plays a major role in determining PDT efficacy, we evaluated the ability of the UCNP@TTD-cRGD NPs to generate $^1\text{O}_2$ under direct NIR light and white light illumination by monitoring the absorbance decrease of 9,10-anthracenediyl-bis(methylene) dimalonic acid (ABDA) at 378 nm (Figure 2E), respectively. Rose Bengal (RB) with a $^1\text{O}_2$ quantum yield of 75% in water was used as the standard photosensitizer [39]. We observed that 980 nm laser illumination of UCNP@TTD-cRGD NPs resulted in an ABDA absorbance decrease at 378 nm, corresponding to $^1\text{O}_2$ generation of TTD encapsulated on the UCNPs' surface (Figure S3A). The initial absorbance of ABDA at 378 nm before illumination is defined as A_0 and the photosensitizer (UCNP@TTD-cRGD NPs or RB) induced ABDA absorbance which decreases at 378 nm after 2 min illumination is defined as A . We observed a linear increase of $\ln(A_0/A)$ over time (Figure 2E). The decomposition rate constants of the UCNP@TTD-cRGD NPs (K_{NPs}) and RB (K_{RB}) were calculated according to the slopes of the linear curves, and determined to be 0.0076 and 0.0176, respectively. The integration ratio of the absorption from 400 to 800 nm between RB (I_{RB}) and UCNP@TTD-cRGD NPs (I_{NPs}), $I_{\text{RB}}/I_{\text{NPs}}$, was calculated to be 1.13. Therefore, the $^1\text{O}_2$ quantum yield of UCNP@TTD-cRGD NPs (Φ_{NPs}) under 980 nm laser illumination was calculated to be 36.4%, which is higher than the $^1\text{O}_2$ quantum yield of the FDA-approved photosensitizer *meso*-tetrahydroxyphenyl-chlorin (mTHPC, $\Phi_{\text{mTHPC}} = 31\%$) [53]. The $^1\text{O}_2$ generation of UCNP@TTD-cRGD NPs under white light illumination was also monitored in Figure S3B and the $^1\text{O}_2$ quantum yield (Φ_{NPs}) was calculated to be 63.7%. However, the higher $^1\text{O}_2$ quantum yield of UCNP@TTD-cRGD NPs under white light illumination as compared to that under 980 nm laser illumination was greatly attenuated after coverage with chicken tissues (Figure S4), as demonstrated in the following study. We further investigated the penetration of a 980 nm laser and white light illumination, using 3 mm and 6 mm thick chicken tissues to mimic clinical skin tissue (Figure S4),

respectively. We observed that the efficiency of $^1\text{O}_2$ generation is significantly decreased (5.1-fold decrease) with white light illumination due to the 3 mm thick chicken tissue coverage, while there is only a 1.0-fold decrease in $^1\text{O}_2$ generation when illuminated at 980 nm (Figure 2F). When the tissue thickness increases to 6 mm, there is barely any $^1\text{O}_2$ generation with white light illumination, while the

generation of $^1\text{O}_2$ could still be detected when illuminated at 980 nm. These results indicate a better penetration depth of 980 nm excitation compared with white light illumination, which makes UCNP@TTD-cRGD NP-based PDT suitable for effective tumor treatment in living systems, especially for deep-seated tumors.

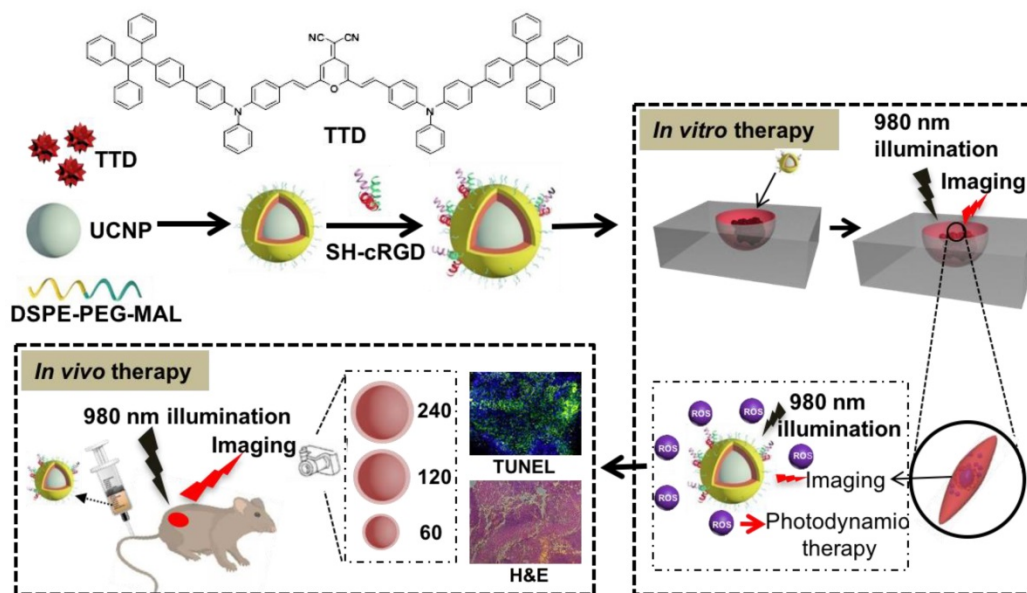


Figure 1. A rational design for a NIR light-regulated theranostic nanoplatform based on AIE luminogen encapsulated upconversion nanoparticles. Schematic illustration of preparation of UCNP@TTD-cRGD nanoparticles and their applications in bioimaging and PDT of deep-seated tumors upon NIR laser illumination, in an *in vitro* three-dimensional (3D) cancer cell spheroid and in a murine tumor model, respectively.

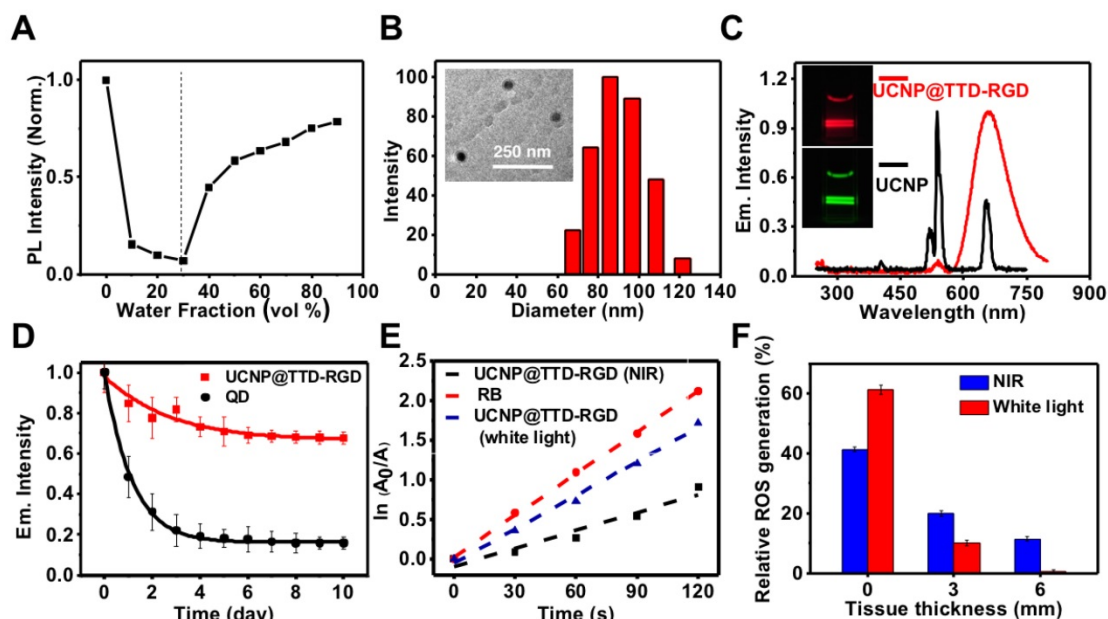


Figure 2. Characterization of the theranostic nanoplatform based on UCNP@TTD-cRGD NPs. (A) Change of PL intensity of 5 μM of TTD in THF-water mixtures with different water fractions (fw %) at the same total volume. (B) Particle size distribution of UCNP@TTD-cRGD NPs studied by dynamic light scattering. Insert image represents the morphology of the UCNP@TTD-cRGD nanoparticle under transmission electron microscopy (the enlarged TEM image can be found in Figure S2). (C) Fluorescence spectra of UCNP and UCNP@TTD-cRGD NPs. (D) Time courses for fluorescence intensity change of UCNP@TTD-cRGD in DMEM supplemented with 10% FBS after continuous incubation at 37 $^{\circ}\text{C}$. (E) Relative ROS generation with Rose Bengal (RB) as the standard photosensitizer (the $^1\text{O}_2$ quantum yield for RB is 75% in water). (F) Relative ROS generation of UCNP@TTD-cRGD excited by NIR or visible light with the coverage of tissues of different thicknesses.

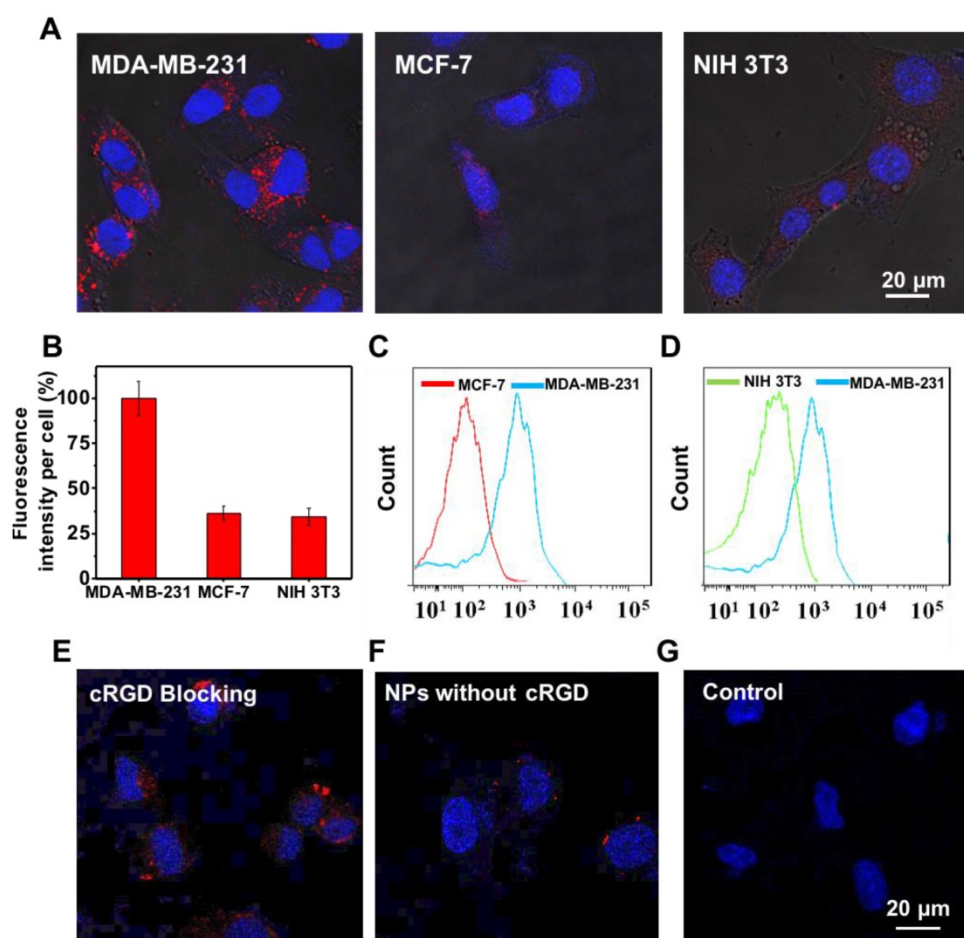


Figure 3. Targeting study of UCNP@TTD-cRGD NPs. (A) Fluorescent images of MDA-MB-231, MCF-7, NIH 3T3 cells after incubation with UCNP@TTD-cRGD NPs ($5 \mu\text{g mL}^{-1}$ of TTD) for 4 h. Red fluorescence is from the UCNP@TTD-cRGD NPs. Blue fluorescence labels the nuclei. (B) Quantitative analysis of fluorescence intensity of UCNP@TTD-cRGD nanoparticle signals from confocal images shown in (A). Flow cytometry results of UCNP@TTD-cRGD nanoparticle-treated MDA-MB-231 cells against MCF-7 cells (C) and NIH 3T3 cells (D), respectively. (E) Confocal images of MDA-MB-231 cells pre-treated with free cRGD before co-incubation of UCNP@TTD-cRGD NPs. (F) Confocal images of MDA-MB-231 cells treated with UCNP@TTD nanoparticles without cRGD conjugation. (G) Confocal images of MDA-MB-231 cells without any treatment. Scale bars: $20 \mu\text{m}$.

Targeting and intracellular ROS detection

Active targeting of NPs to cancer cell-specific receptors could promote rapid intracellular uptake of the enhanced permeability and retention (EPR) accumulated nanoformulations. To examine the targeting ability of UCNP@TTD-cRGD NPs, the $\alpha_v\beta_3$ integrin overexpressed MDA-MB-231 cells were used as integrin-positive cancer cells, using MCF-7 and NIH 3T3 cells as the negative controls. The MDA-MB-231 cells, MCF-7 and NIH 3T3 cells were incubated with UCNP@TTD-cRGD NPs ($5 \mu\text{g mL}^{-1}$ of TTD) for 4 h and then imaged using a confocal microscope (Figure 3A). We observed clear red fluorescence from the UCNP@TTD-cRGD NPs in the cytoplasm of the MDA-MB-231 cells, but much lower signals in the MCF-7 and NIH 3T3 cells (Figure 3A). We also quantified the fluorescence intensity using the ImageJ program from confocal images and set the fluorescence intensity of the MDA-MB-231 cells at 100% (Figure 3B). We observed that the fluorescence

intensity of MCF-7 and NIH 3T3 cells was only 36.3% and 34.4%, respectively. We also performed a flow cytometry study to further evaluate the targeting capability of UCNP@TTD-cRGD NPs on MDA-MB-231 cells. We observed that the mean fluorescence intensity of MDA-MB-231 cells was significantly higher than that of the MCF-7 and NIH 3T3 cells (Figure 3C-D). The results indicate that UCNP@TTD-cRGD NPs can be selectively internalized by MDA-MB-231 cells in significant quantities, demonstrating the targeting capability of UCNP@TTD-cRGD NPs. Besides, the uptake of UCNP@TTD-cRGD NPs by cRGD pre-treated MDA-MB-231 cells was significantly suppressed as shown in Figure 3E. Moreover, the UCNP@TTD NPs without cRGD conjugation could not be effectively internalized by the MDA-MB-231 cells (Figure 3F). These results clearly suggest that the targeting capability of UCNP@TTD-cRGD NPs is mainly due to the cRGD conjugation on the particle surface.

It has been well accepted that the loss of cell viability induced by PDT is associated with excessive intracellular ROS production. To evaluate the intracellular ROS production of UCNP@TTD-cRGD NPs under NIR laser illumination, we used the CellROX® Deep Red Reagent as the intracellular ROS indicator. After oxidation by ROS, CellROX® Deep Red reagent becomes fluorescent at 633 nm laser illumination. As shown in **Figure 4**, excessive intracellular ROS generation was observed in the cytoplasm of MDA-MB-231 cells treated with UCNP@TTD-cRGD NPs and 980 nm laser illumination (**Figure 4A**) as compared to the MDA-MB-231 cells with only 980 nm laser illumination (**Figure 4B**). The results demonstrate the robust capability of UCNP@TTD-cRGD NPs in producing intracellular ROS under NIR light regulation.

***In vitro* PDT efficiency of UCNP@TTD-cRGD NPs**

The potential photodynamic cytotoxicity of UCNP@TTD-cRGD NPs was further evaluated through an *in vitro* cytotoxicity assay (**Figure 5A**). We observed that without 980 nm laser illumination, there is negligible cytotoxicity in the UCNP@TTD-cRGD NP-treated MDA-MB-231, MCF-7 and NIH 3T3 cells in a 50 µg/mL concentration, suggesting a minimum cytotoxicity caused by the NPs. However, with 980 nm laser illumination (200 mW cm⁻², 2 min) and white light illumination (200 mW cm⁻², 2 min), only 28.3% and 16.6% of the MDA-MB-231 cells treated with UCNP@TTD-cRGD NPs (25 µg/mL, or 5 µg mL⁻¹ of TTD) remained alive, respectively. Yet the

viability of the MCF-7 and NIH 3T3 cells was not significantly affected by the NP treatment, demonstrating the robust capability of UCNP@TTD-cRGD NPs in selectively killing MDA-MB-231 cells under both 980 nm laser and white light illumination (**Figure 5B**). In addition, we found that 2 min 980 nm laser illumination does not affect the cell viability of all the cells without NP treatment, further confirming that the acute cytotoxicity is only induced by the internalized UCNP@TTD-cRGD NPs under light illumination. The live/dead staining results demonstrate that most MDA-MB-231, MCF-7 and NIH 3T3 cells treated with NPs or 2 min 980 nm laser illumination alone are still alive, as revealed by the green fluorescence in **Figure 5C**. However, nearly all the UCNP@TTD-cRGD NP-incubated MDA-MB-231 cells were dead under 980 nm laser illumination or white light illumination, as indicated by the red fluorescence in **Figure 5C**, demonstrating the effectiveness of UCNP@TTD-cRGD NPs in selectively killing MDA-MB-231 cells. Furthermore, the laser output power and exposure time to obtain a significant antitumor efficacy in our technique (200 mW cm⁻², 2 min) is much lower and shorter than that needed in the previous study (3 W cm⁻², 10 min) which also used AIE-encapsulated UCNPs for cancer PDT [54]. Collectively, the synthesized UCNP@TTD-cRGD NPs can selectively light up the MDA-MB-231 cells and then kill the MDA-MB-231 cells by elevating intracellular ROS generated from the UCNP@TTD-cRGD NPs under NIR light illumination.

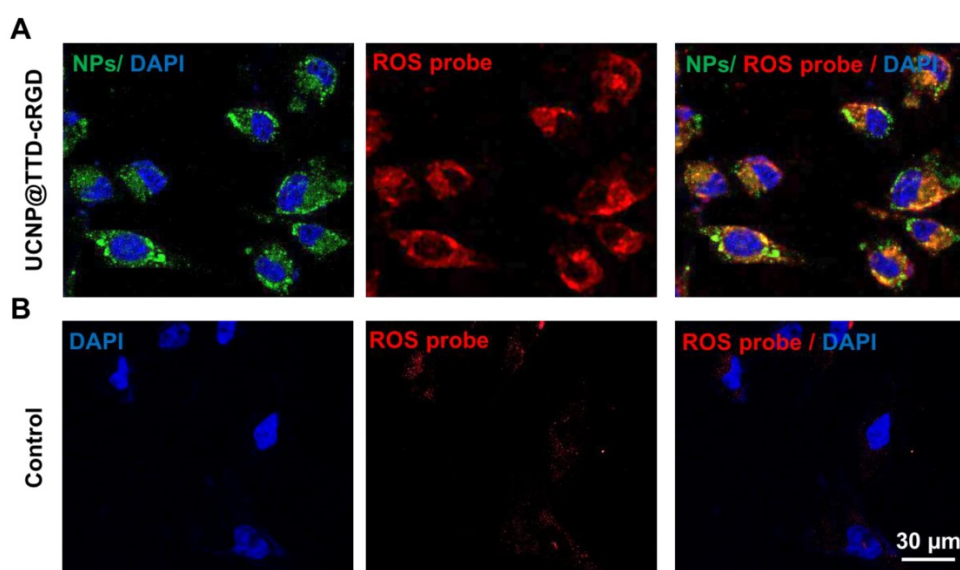


Figure 4. Intracellular ROS generation of UCNP@TTD-cRGD NPs. (A) Detection of intracellular ROS generation in living MDA-MB-231 cells after co-culture with UCNP@TTD-cRGD NPs (5 µg mL⁻¹ of TTD) and CellROX® Deep Red reagent, followed by light illumination ($\lambda_{\text{ex}} = 980 \text{ nm}$; 530/25 nm bandpass filter). The red fluorescent signals represent the intracellular ROS. (B) Detection of intracellular ROS generation in living MDA-MB-231 cells only with NIR laser (980 nm) illumination.

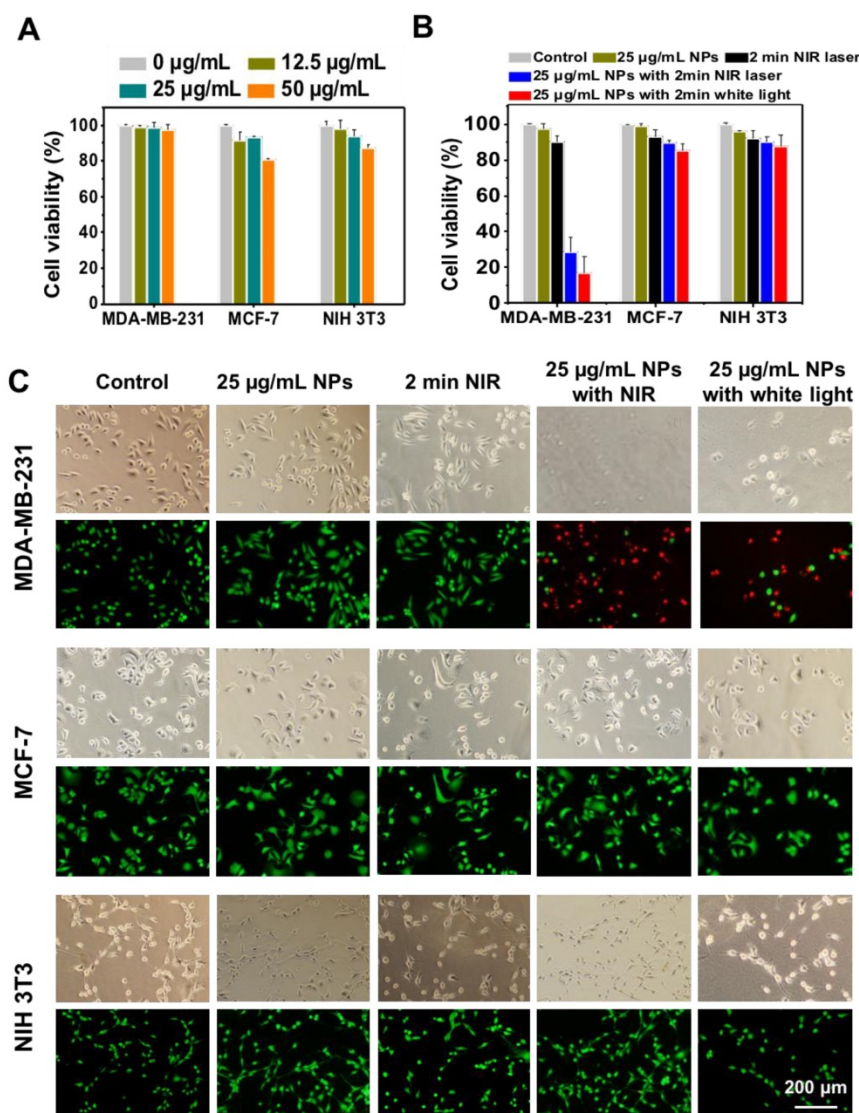


Figure 5. Cytotoxicity study of UCNP@TTD-cRGD NPs with or without light illumination. (A) Cell viabilities of UCNP@TTD-cRGD nanoparticle-treated MDA-MB-231 cells, MCF-7 cells and NIH 3T3 cells without light or NIR laser irradiation. **(B)** Viability of MDA-MB-231, MCF-7 and NIH 3T3 cells after incubation with UCNP@TTD-cRGD NPs (5 µg mL⁻¹ of TTD) for 4 h followed by 980 nm laser or light irradiation (100 mW cm⁻², 2 min). **(C)** Live/dead staining after NIR laser PDT treatment.

Since 2D *in vitro* tumor models usually cannot predicate the *in vivo* outcomes because of their oversimplification and non-representation of 3D natural tissues [55], we further investigated the therapeutic effect of UCNP@TTD-cRGD NPs as a PDT agent for tumor therapy in a 3D *in vitro* tumor model (Figure 6A). We observed that contrary to the PDT outcomes observed in the 2D model, prolonged illumination durations up to 30 min are required to kill ~70% of the cells from the 3D cell spheroids (Figure 6B). The metabolic activity of the cell spheroids after PDT treatment was evaluated by MTT assay, after further culture for 5 days. We observed that the viability of the 3D cell spheroid declined to 60.5% after 30 min of 980 nm laser illumination (Figure 6C). The bright field images and F-actin

staining of the 3D cell spheroids demonstrate the clear disruption of the 3D cell spheroid under NIR light-regulated PDT (Figure S5).

To study the mechanism of PDT using UCNP@TTD-cRGD NPs in killing MDA-MB-231 cells, we used APC Annexin V/Dead Cell Apoptosis Kit to stain the PDT-treated cells for flow cytometry evaluation (Figure 7). We observed that after 12, 24 and 48 h incubation, the apoptosis rate was 20.5%, 54.5% and 12.2% (Figure 7A), respectively and the corresponding necrosis rate was 12.5%, 24.2% and 78.9%, respectively. The result demonstrates a clear apoptosis-to-necrosis process for cells with PDT treatment. The confocal images showed that the intracellular NPs (yellow) are encapsulated by a damaged cell membrane as revealed by the red

fluorescence (Figure 7B), while no fluorescence is observed in the untreated MDA-MB-231 cells (Figure S6A), confirming that cell apoptosis is the mechanism in NIR light-regulated PDT. We further studied the

cell apoptosis under different illumination durations (such as 0, 2, 5, and 10 min) and found that a prolonged illumination time can promote cell apoptosis to necrosis (Figure S6B).

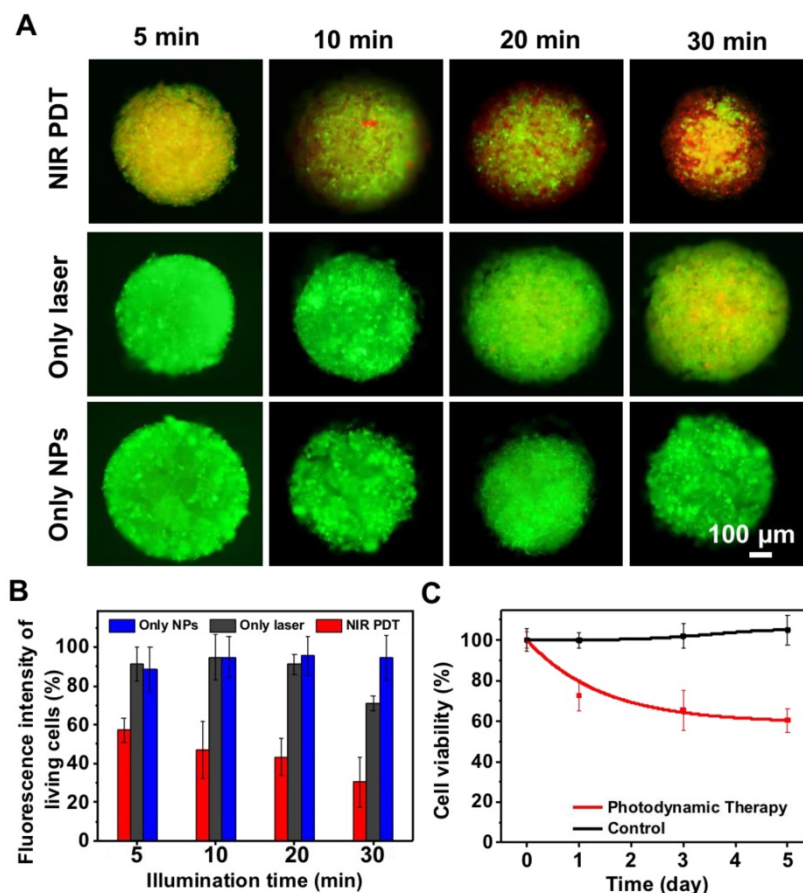


Figure 6. The evaluation of UCNP@TTD-cRGD NPs in cancer therapy using an *in vitro* 3D cancer model. (A) Live/dead staining of cell spheroids irradiated with a 980 nm laser. (B) Quantitative analysis of live/dead fluorescence signals in each cell spheroid shown in (A). (C) The viability of cell spheroids after NIR light PDT treatment revealed by MTT study.

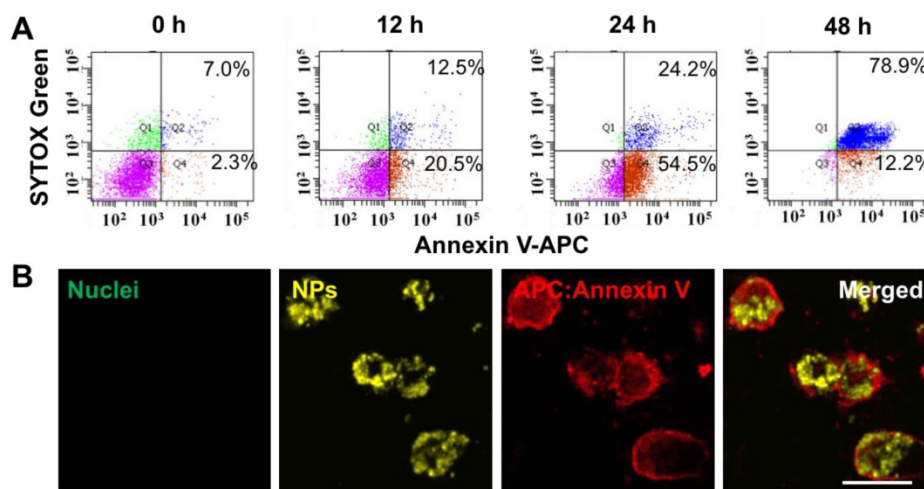


Figure 7. Apoptosis and necrosis staining of MDA-MB-231 cells after PDT based on UCNP@TTD-cRGD NPs. (A) Flow cytometry results for the MDA-MB-231 cells after co-culture with UCNP@TTD-cRGD NPs (5 µg mL⁻¹ of TTD) for 4 h at 37 °C and then exposed to 2 min of 980 nm laser illumination (100 mW cm⁻²), following by further incubation for 12, 24 and 48 hours, respectively. Then, the apoptosis/necrosis was accessed with APC Annexin V/Dead Cell Apoptosis Kit staining by flow cytometry. (B) Confocal images of MDA-MB-231 cells treated with PDT and continuously cultured for 12 h are shown. The green fluorescence signal in the left image from the SYTOX® Green (λ_{ex} = 488 nm; 520/20 nm bandpass filter) was used to stain the nucleus of the necrotic cells. The yellow fluorescence signal was from UCNP@TTD-cRGD NPs (λ_{ex} = 488 nm; 585/20 nm bandpass filter). The red fluorescence signal was from APC annexin V (λ_{ex} = 633 nm; 660/20 nm bandpass filter).

In vivo antitumor efficacy of UCNP@TTD-cRGD NPs

Inspired by the promising imaging and PDT results in both *in vitro* 2D and 3D cancer models, we then examined the *in vivo* theranostic efficacy of UCNP@TTD-cRGD NPs for treatment of deep-seated tumors via intratumoral injection of UCNP@TTD-cRGD NPs into living female Balb/c nude mice (**Figure 8**). Instead of covering a piece of tissue over the subcutaneous tumor to represent deep-seated tumors, we grew MDA-MB-231 tumors with different initial therapeutic tumor volumes including 60 mm³ (widely used as the initial therapeutic tumor size), 120 mm³ and 240 mm³, respectively. We used the enlarged initial therapeutic tumor volumes (120 mm³ and 240 mm³) for the deep-seated tumors which are more relevant to the tumors seen in clinical practice as compared to covering a piece of tissue over the subcutaneous tumor. We found that the intratumorally injected UCNP@TTD-cRGD NPs with bright fluorescence can clearly reveal the boundary of the tumors for at least 7 days (**Figure 8A**). After 7 days, we obtained the tumor and major organs of the mice with intratumorally injected UCNP@TTD-cRGD NPs. We observed that most NPs were still within the tumors, while only a few NPs were metabolized by the liver (**Figure 8B**). The results indicate the excellent internalization and retention of UCNP@TTD-cRGD NPs at the tumor sites, which favors long-term tumor imaging and tumor treatment by PDT. Furthermore, we investigated the therapeutic effect of UCNP@TTD-cRGD NPs as a PDT agent for deep-seated tumor therapy in living mice by dividing the tumor-bearing mice into three groups based on their initial tumor volumes (60 mm³, 120 mm³ and 240 mm³). In each group, there were five sub-groups including the laser PDT group, white light PDT group, laser-only group, nanoparticle-only group and control group. In the laser PDT group (n=6), UCNP@TTD-cRGD NPs were injected into the implanted tumor, and followed by a 980 nm laser illumination on the tumors after intratumoral injection for 4 h. The tumor-bearing mice in the white light PDT group (n = 6) were irradiated with white light under identical conditions. Tumor-bearing mice with injection of only UCNP@TTD-cRGD NPs but no NIR or white light illumination were assigned to be the nanoparticle-only group (n = 6). In the laser-only group (n = 6), the tumor-bearing mice were only irradiated with a 980 nm laser. The mice in the control group (n = 6) were injected with saline only. To minimize the overheating effect of 980 nm laser illumination, we used a transparent ice bag to cover

the tumors for the 980 nm laser illumination. The tumor sizes in the different groups were measured to assess the PDT efficacy over a period of 10 days.

In the group with an initial tumor volume of 60 mm³, both NIR-regulated PDT treatment ($P \leq 0.001$) and white light-regulated PDT treatment ($P \leq 0.009$) could significantly inhibit tumor growth as compared with that observed in other groups, thus confirming the capability of UCNP@TTD-cRGD NPs in killing cancer cells (**Figure 8C**). Importantly, the growth of tumors in the laser PDT group was significantly restricted as compared to that in the white light PDT group, indicating the superior capability of NIR light-regulated PDT in enhancing therapeutic outcomes, due to the deep tissue penetration of NIR light and the successful energy transfer between the UCNPs and TTD (**Figure 8C**). On the other hand, the tumors in the laser-only group, nanoparticle-only group and control group grew in an exponential manner over the period of time, suggesting that the treatment with 980 nm laser only or UCNP@TTD-cRGD NPs without light illumination induces minimum inhibition of tumor growth.

In the group with an initial tumor volume of 120 mm³, the therapeutic outcomes of white light-regulated PDT treatment ($P \leq 0.016$) were sub-optimal as revealed by the limited tumor shrinkage ratio (30%, reduced tumor volume in PDT group/tumor volume in control group). However, the shrinkage ratio of tumors with an initial tumor volume of 60 mm³ after white light-regulated PDT treatment (**Figure 8D**) was around 60%. However, NIR-regulated PDT treatment ($P \leq 0.001$) could still obviously inhibit tumor growth as compared with other groups, demonstrating the robust capability of UCNP@TTD-cRGD NPs in killing cancer cells under NIR light illumination (**Figure 8D**). When the initial tumor volume increased to 240 mm³, white light PDT treatment could not inhibit tumor growth anymore, as indicated by the same tumor growth rate in the white light PDT group, laser-only group, nanoparticle-only group and control group (**Figure 8E**). However, tumor growth in the 980 nm laser PDT group could still be obviously restricted, confirming the great potential of UCNP@TTD-cRGD NPs in treating deep-seated tumors under NIR light illumination (**Figure 8E**).

To further evaluate the therapeutic efficacy against deep-seated tumors, we also performed TUNEL and H&E staining using the tissue sections from the laser PDT group and white light PDT group after 10 days (**Figure 8F** and **Figure S7**), respectively. These tissue sections from each isolated tumor were further divided based on their layers (upper, middle and bottom) within the tumor. We observed that in

the group comprising initial tumor volumes of 60 mm³, both laser PDT and white light PDT can induce cancer cell apoptosis in the bottom layers of the tumors (Figure 8F). However, when the initial tumor volume becomes 120 and 240 mm³, white light PDT can only induce apoptosis of cancer cells in the middle and upper layers, respectively, due to the limited tissue penetration of the white light. In contrast, NIR light-regulated PDT treatment can still cause apoptosis of cells in the corresponding deeper layers, further confirming the potential of UCNP@TTD-cRGD NPs in treating deep-seated tumors under NIR light illumination. H&E staining results demonstrate

the same superior therapeutic outcomes of NIR light-regulated PDT as compared to white light-regulated PDT in tumors from the different groups (60 mm³, 120 mm³ and 240 mm³) (Figure S7). In addition, the weight of all mice could be maintained within a healthy range (Figure S8A) and the tumors under NIR laser-regulated PDT treatment had a small tumor weight (Figure S8B). These results clearly imply that the UCNP@TTD-cRGD NPs accompanied by laser illumination at 980 nm could serve as a reliable platform for effective *in vivo* deep-seated tumor treatment.

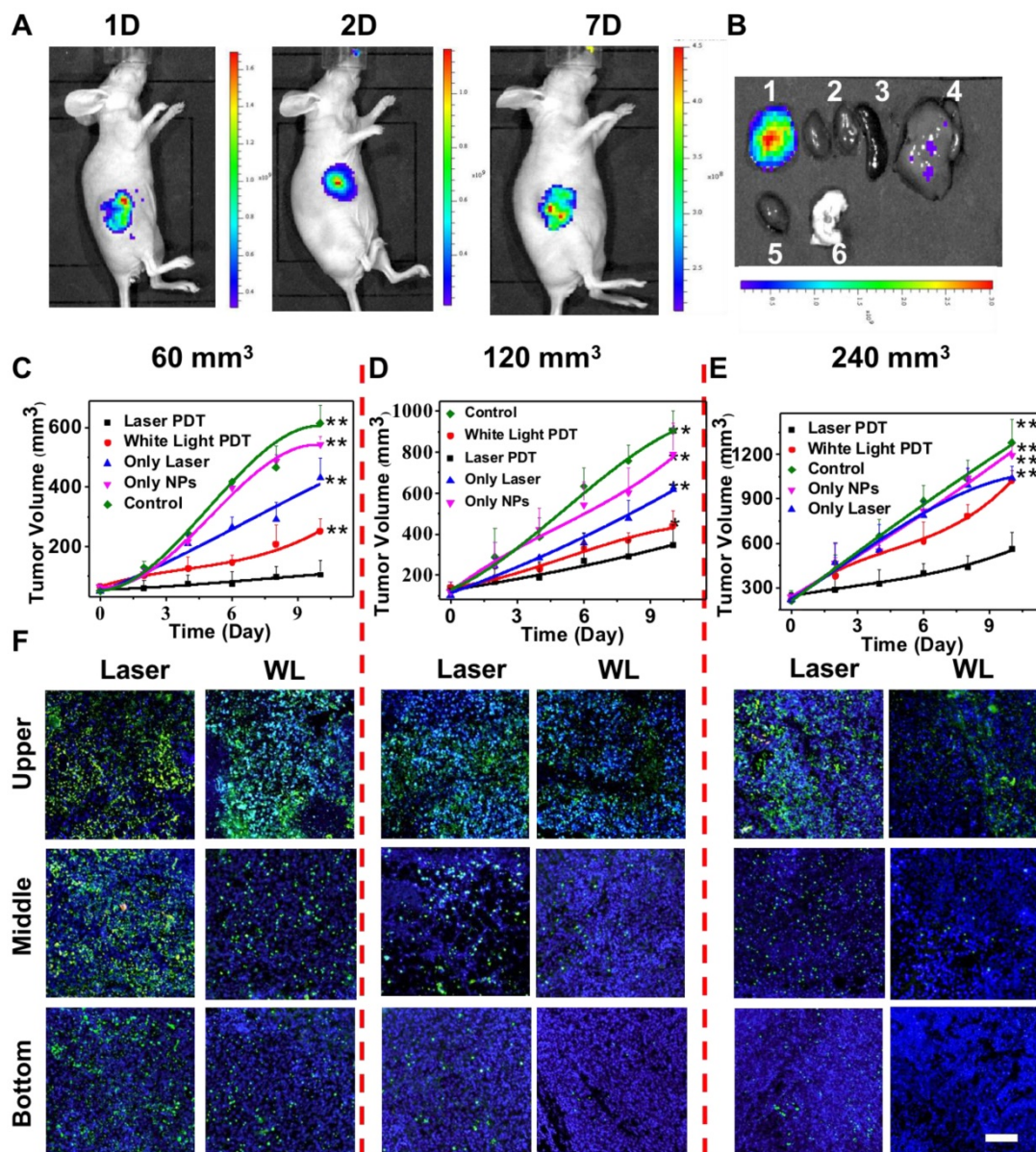


Figure 8. *In vivo* fluorescence imaging and PDT efficiency by intratumoral injection of UCNP@TTD-cRGD NPs. (A) The *in vivo* fluorescence images of the tumor after being intratumorally injected with UCNP@TTD-cRGD NPs for 1, 2 and 7 days. (B) *Ex vivo* fluorescence imaging of the tumor and organs harvested from the euthanized mice with intratumoral injection of nanoparticles after administration for 7 days (1 Tumor, 2 Kidney, 3 Spleen, 4 Liver, 5 Heart and 6 Lung). Growth curves of tumors in laser PDT, white light PDT, nanoparticle-only, laser-only and control groups with initial tumor volumes of 60 (C), 120 (D) and 240 mm³ (E), respectively. (F) TUNEL staining results of tumor slices collected from mice that were divided by their initial tumor volumes of 60, 120 and 240 mm³, respectively. *P < 0.05, **P < 0.01.

To study whether cRGD conjugation can aid in tumor uptake in living mice, we used fluorescence imaging to monitor in real time the targeting effect of UCNP@TTD-cRGD NPs *in vivo* (Figure 9A). The fluorescent images were recorded at different time intervals after the first intravenous injection of UCNP@TTD-cRGD NPs. We observed that the NPs reveal a time-dependent biodistribution and tumor preferential profile in the mice. At 0 h, the intense fluorescence near the tail reveals the presence of NPs at the tail vein after intravenous injection. We observed that there was a significant increase in fluorescence in the tumor of living mice at 4 h post-injection of UCNP@TTD-cRGD NPs (Figure 9A) and then the fluorescence reached the highest level in the tumor at 8 h post-injection. Then the fluorescent signals gradually decreased at 24 h post-injection in the circulation process. The weak fluorescence at the neck reveals the potential presence of NPs at the lymph nodes [56]. The biodistribution result demonstrates that the NPs are mainly accumulated in the liver (Figure 9B), which agrees with previous findings [57, 58]. Methods such as saturating the

receptors of Kupffer cells which are responsible for the majority of phagocytic activity in the liver, with decoy and nontoxic nanoparticles prior to administration of nanotherapeutics [59], and coating the membrane of cells (such as red blood cells, leukocytes, and monocytes) have been designed to reduce nanoparticle entrapment by the liver [60-62], thus enhancing the delivery of therapeutic NPs to the diseased tissues. The quantity of NPs accumulating at the tumor site is still much higher than that in other organs such as the kidney, heart, lung, and spleen (Figure 9B and Figure S9), indicating the *in vivo* targeting capability of UCNP@TTD-cRGD NPs. To further evaluate the *in vivo* targeting specificity of the UCNP@TTD-cRGD NPs, we first intravenously injected free cRGD (15 mg kg⁻¹) into MDA-MB-231 tumor bearing mice. At 30 min post-injection, we then intravenously injected the same dose of UCNP@TTD-cRGD NPs. We found that the uptake of UCNP@TTD-cRGD NPs at 24 h post-injection by the tumor pretreated with cRGD was significantly inhibited (Figure 9C), demonstrating the *in vivo* targeting specificity of UCNP@TTD-cRGD NPs.

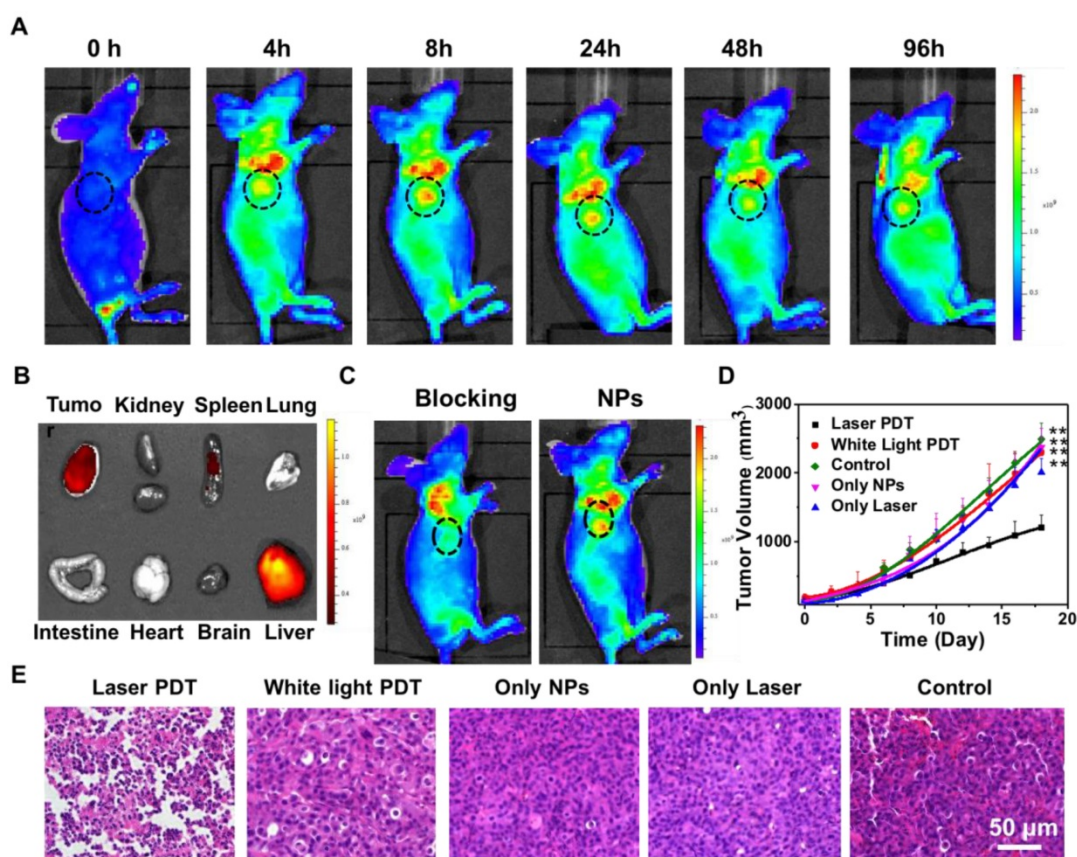


Figure 9. *In vivo* targeted tumor imaging and PDT therapy by intravenous injection of UCNP@TTD-cRGD NPs. (A) Biodistribution of UCNP@TTD-cRGD NPs in tumor-bearing mice after intravenous injection of UCNP@TTD-cRGD NPs (30 mg/kg) at different times. Black circles indicate the tumor. (B) Ex vivo fluorescence imaging of various organs and tumor tissues from mice intravenously injected with UCNP@TTD-cRGD NPs. The mice were sacrificed at 12 h post-injection. (C) Biodistribution of UCNP@TTD-cRGD NPs in tumor-bearing mice 8 h after intravenous injection of UCNP@TTD-cRGD NPs (30 mg/kg) without or with blocking the receptors. Red circles indicate the tumor. (D) Growth curves of tumors in laser PDT, white light PDT, nanoparticle-only, laser-only and control groups, respectively, and nanoparticles were intravenously injected into tumors with an initial tumor volume of 120 mm³. (E) H&E staining results of tumor slices collected from different groups of mice. **P < 0.01.

Encouraged by the imaging data that revealed the effective tumor uptake of UCNP@TTD-cRGD NPs, we continued the light-mediated PDT therapy via intravenous injection of UCNP@TTD-cRGD NPs or saline into five different groups of mice with an initial tumor volume of 120 mm³. As shown in **Figure 9D**, after 980 nm laser illumination, the growth rate of the tumors in the laser PDT group (n = 6, P ≤ 0.01) was found to be restricted significantly over the therapeutic period, whereas the tumors in the white PDT group, laser-only group, nanoparticle-only group and control group (n = 6) revealed a fast growth rate. Further increase in the NP injection times and light irradiation times could improve the therapeutic outcome to realize complete cancer ablation. These data suggest that the facilitated tumor uptake by cRGD and effective tumor reduction is mainly due to the production of ¹O₂ from the TTD encapsulated UCNPs under 980 nm laser illumination.

In addition to the promising antitumor therapy *in vivo*, the histological tumor tissue analysis also reveals the efficacy of the PDT treatment. After 10 days of light-mediated PDT at 980 nm, H&E and TUNEL staining of the tumor tissues displayed more significant damage in the mice with intravenous injection of UCNP@TTD-cRGD NPs than those tumors treated in the other groups (**Figure 9E**). Moreover, there was no obvious hemolysis and organ damage observed during the treatment (**Figure S10**). These results clearly indicate that UCNP@TTD-cRGD NPs hold great potential for improving the therapeutic efficacy of *in vivo* deep-seated tumor treatment with a desirable PDT outcome.

Discussion

Photodynamic antitumor therapy has been widely applied in the clinical treatment of various types of cancers such as lung cancer, gastrointestinal cancer, head and neck tumor and prostate tumors [14], due to its distinct advantages which include precise controllability, a minimally invasive nature and high spatiotemporal accuracy compared with conventional chemotherapy [63, 64]. However, its application in treating deep-seated tumors is restricted due to the shortcomings of classical PSs such as poor solubility and aggregation under physiological conditions, undesirable pharmacokinetics, and low tumor selectivity. In contrast, NP-based PDT has emerged as an extremely promising avenue for future technological breakthroughs. NPs can transport hydrophobic PSs in a high PS “payload” to the tumor site via an enhanced permeability and retention (EPR) effect. Additional surface modification and functionalization with

targeting moieties could further enhance the selective accumulation of the PS loaded NPs at the target site.

However, NP-based PDT still suffers from drawbacks such as the severe aggregation of hydrophobic PSs, which have an ACQ property, and the therapeutic efficiency of ACQ PSs is dependent on their aggregation state. To solve the aggregation-caused fluorescence and ROS reduction of ACQ PSs [14], AIEgen PSs with the remarkable feature of generating ROS and fluorescent signals even in the aggregated state have been developed as a better choice for image-guided PDT with improved therapeutic outcomes [26, 65]. In particular, inspired by exactly the opposite photophysical properties of AIEgen PSs and ACQ PSs in the aggregated and monomeric states, the ACQ PS (pheophorbide-a) and AIEgen PS (tetraphenylsilole) have been encapsulated into a pH-responsive nanoprobe that can realize activated photodynamic ablation of cancer cells with limited side effects, and *in situ* prediction of the therapeutic response [66]. Various AIEgen PSs with NIR emission have been developed for cancer theranostics [28, 67-69]. However, these reported AIEgen PSs are excited in a UV-visible wavelength ranging from 378 to 600 nm, which unfortunately shows limited penetration depth in biological tissues [70]. Efforts have been devoted to developing AIEgen PSs that can be excited by red or NIR light [17, 71]. However, the preparation of red/NIR fluorescent molecules is extremely complicated regardless of either the AIEgens or conventional dyes [72, 73], which usually require several-step reactions and inconvenient purifications. Recently, AIEgen PSs with high two-photon absorption (TPA) have been developed for PDT of deep-seated tumors. However, the TPA protocol requires the use of a tightly focused femtosecond laser beam as a light source to excite a small focused area and obtain sufficient instant energy for two-photon excitation [74, 75]. Moreover, TPA materials often suffer from severely decreased quantum yields after transfer into water through molecular engineering or nanoparticle formulation [74]. Therefore, there is an urgent need to develop a facile and effective method for fabrication of a NIR light activated PDT platform based on AIEgens.

Lanthanide-doped UCNPs with an intrinsic photon-converting nature upon exposure to long-wavelength light illumination have received considerable attention in cancer imaging and therapy [5, 63]. These UCNPs are excited by NIR light and can emit fluorescence across UV, vis, or even the NIR range in accordance with the absorption characteristics of PSs. Recently, various UCNPs have been loaded with PSs (such as chlorin e6 and β-carboxyphthalocyanine zinc) to engineer a

NIR-triggered cancer theranostic nanoplatform for cancer treatment [63, 76-78]. However, these PSs generally suffer from ACQ, which restricts their therapeutic efficiency. Therefore, the combination of UCNPs and AIEgen PSs [70] which usually require visible light excitation provides a facile and effective way to fabricate a NIR light activated PDT nanoplatform based on AIEgen PSs. Although, the combination of UCNPs with AIEgen PS for *in vitro* PDT treatment of cancer cells was attempted once [54], the ultra-small UCNPs that were used (< 12 nm) as the NIR light “transducer” suffered from a significant decrease in upconversion emission intensity and luminescence lifetime as compared with UCNPs with a larger particle size (> 40 nm), due to the severe surface quenching [79, 80]. Moreover, the severe aggregation of the synthesized particles hampers their blood circulation and diffusion of ROS generated in the inner part of the aggregates because of the severely small active radius of the ROS (< 20 nm) [48], which leads to the dramatic decrease in both *in vitro* and *in vivo* PDT efficiency. Therefore, a NIR light-regulated cancer theranostic nanoplatform with bright emission, high ROS production and good monodispersity is highly desired to successfully treat deep-seated tumors.

In this research work, we encapsulated AIEgen PS TTD and NaYF₄:Yb,Er UCNPs using amphiphilic polymers and then conjugated cRGD on the particle surface to yield UCNP@TTD-cRGD NPs. The TTD and UCNP within the NP core could be densely packed together because of the hydrophobic interactions between TTD and the UCNPs, which favor energy transfer between these two components, approved by experimental results. Therefore, the higher singlet oxygen production with 980 nm illumination in the presence of tissue coverage compared with the white light illumination makes UCNP@TTD-cRGD NP-based PDT suitable for deep-seated tumor treatment in living systems. Compared with two-photo excitation which also possesses deep tissue-penetration ability, upconversion processes are more efficient, and they can be realized using inexpensive continuous-wave (CW) lasers, unlike two-photon excitation, which requires pulsed lasers [81]. Our extensive *in vitro* and *in vivo* fluorescence imaging studies validated the successful active targeting, which can be easily recognized by the enhanced fluorescence intensity within the targeted cancer cells and the *in vivo* tumors. Both *in vitro* and *in vivo* theranostic studies successfully demonstrated that such AIEgen PS-encapsulated UCNPs with NIR laser activation could significantly inhibit tumor growth in PDT treatment compared to those AIEgen PSs excited

under white light. With the rapid development of synthetic and theoretical approaches, the emission range of UCNPs can be easily tuned by the type and amount of ions doped, which is advantageous in the selection of available AIEgen PSs as photosensitizing agents in this protocol [64]. Thus, a therapeutic nanoplatform based on AIEgen PS-encapsulated UCNPs is emerging as a versatile tool for deep-seated tumor therapy. It is known that the upconversion efficiency from NIR light to UV/vis light of UCNP is low, which reduces the singlet oxygen generation quantum yield of UCNP@TTD-cRGD NPs. Methods such as the homogeneous doping based on a successive layer-by-layer approach [82], suppressing surface quenching effects via heteroepitaxial growth of a biocompatible CaF₂ shell [83], and coupling UCNPs with an organic NIR dye molecule [84] have been developed to increase the upconversion efficiency of UCNPs. A 100-time enhancement in the upconversion efficiency of NaYbF₄:Tm@NaYF₄:Nd UCNPs has been achieved by their coupling with a NIR sensitive organic dye [84]. Therefore, a NIR-regulated cancer theranostic nanoplatform engineered by encapsulating UCNPs and AIEgen PSs with improved singlet oxygen generation quantum yield can be realized to achieve excellent PDT efficacy. It should be noted that the generation of ROS is highly oxygen-dependent, which will limit the therapeutic effect of PDTs in treating hypoxic tumors [85]. Integration of an oxygen supplier (perfluorohexane) [86, 87] or oxygen-independent radical source [88], within the NIR light-regulated cancer theranostic nanoplatform could be the solution for expanding its application in treating hypoxic tumors.

Conclusion

In summary, the synthesized UCNP@TTD-cRGD NPs showed great potential for NIR light-regulated photodynamic therapy of deep-seated tumors. With high photostability, the UCNP@TTD-cRGD NPs could maintain their fluorescent intensity above 70% after 30 days, and under NIR light illumination, a significant amount of ROS could still be detected even with coverage with a 6 mm tissue. The UCNP@TTD-cRGD NPs could specifically target $\alpha_v\beta_3$ integrin overexpressed MDA-MB-231 cells and selectively kill these cells in both 2D and 3D cancer models upon NIR light illumination, without obvious dark cytotoxicity. The results of *in vivo* antitumor evaluation demonstrated that with NIR light illumination, the intravenously injected UCNP@TTD-cRGD NPs could light up the tumors and significantly induce apoptosis of tumor cells, and thus inhibit the growth of large tumors in a mouse model compared to white light illumination. The potential for

UCNP@TTD-cRGD NPs in NIR light-regulated imaging and therapy of deep-seated tumors will inspire further exploration of novel theranostic nanoplatfoms through the combination of UCNPs with various AIEgen PSs for the advancement of deep-seated tumor treatment allowing for strong potential clinical translation.

Supplementary Material

Supplementary figures.

<http://www.thno.org/v09p0246s1.pdf>

Acknowledgements

This work was financially supported by the National Natural Science Foundation of China (31600804, 11522219, 11532009), the Natural Science Basic Research Plan in Shaanxi Province of China (2017JQ3035, 2015JQ1009), the China Postdoctoral Science Foundation funded project (2018T111071, 2016M592799), and the Fundamental Research Funds for the Central Universities (xjj2016081).

Competing Interests

The authors have declared that no competing interest exists.

References

- Umar A, Dunn BK, Greenwald P. Future directions in cancer prevention. *Nat Rev Cancer*. 2012; 12: 835-48.
- Morrissey AS, Garzia L, Shih DJH, Zuyderduyn S, Huang X, Skowron P, et al. Divergent clonal selection dominates medulloblastoma at recurrence. *Nature*. 2016; 529: 351-7.
- Taratula O, Schumann C, Duong T, Taylor KL, Taratula O. Dendrimer-encapsulated naphthalocyanine as a single agent-based theranostic nanoplatfom for near-infrared fluorescence imaging and combinatorial anticancer phototherapy. *Nanoscale*. 2015; 7: 3888-902.
- Mehanna H, Wong W-L, McConkey CC, Rahman JK, Robinson M, Hartley AGJ, et al. PET-CT Surveillance versus Neck Dissection in Advanced Head and Neck Cancer. *New Engl J Med*. 2016; 374: 1444-54.
- Idris NM, Gnanasammandhan MK, Zhang J, Ho PC, Mahendran R, Zhang Y. In vivo photodynamic therapy using upconversion nanoparticles as remote-controlled nanotransducers. *Nat Med*. 2012; 18: 1580-5.
- Castano AP, Mroz P, Hamblin MR. Photodynamic therapy and anti-tumour immunity. *Nat Rev Cancer*. 2006; 6: 535-45.
- Wang D, Fei B, Halig LV, Qin X, Hu Z, Xu H, et al. Targeted Iron-Oxide Nanoparticle for Photodynamic Therapy and Imaging of Head and Neck Cancer. *ACS Nano*. 2014; 8: 6620-32.
- Gohy J-F, Zhao Y. Photo-responsive block copolymer micelles: design and behavior. *Chem Soc Rev*. 2013; 42: 7117-29.
- Yu G, Yang Z, Fu X, Yung BC, Yang J, Mao Z, et al. Polyrotaxane-based supramolecular theranostics. *Nat Commun*. 2018; 9: 766.
- Yu G, Zhao X, Zhou J, Mao Z, Huang X, Wang Z, et al. Supramolecular Polymer-Based Nanomedicine: High Therapeutic Performance and Negligible Long-Term Immunotoxicity. *J Am Chem Soc*. 2018; 140: 8005-19.
- Zhou J, Zhang Y, Yu G, Crawley MR, Fulong CRP, Friedman AE, et al. Highly Emissive Self-Assembled BODIPY-Platinum Supramolecular Triangles. *J Am Chem Soc*. 2018; 140: 7730-6.
- v. Bünau G. J. B. Birks: Photophysics of Aromatic Molecules. Wiley-Interscience, London 1970. 704 Seiten. Preis: 210s. Berichte der Bunsengesellschaft für physikalische Chemie. 1970; 74: 1294-5.
- Sekkat N, Bergh Hvd, Nyokong T, Lange N. Like a Bolt from the Blue: Phthalocyanines in Biomedical Optics. *Molecules*. 2012; 17: 98-144.
- Lucky SS, Soo KC, Zhang Y. Nanoparticles in Photodynamic Therapy. *Chem Rev*. 2015; 115: 1990-2042.
- Punjabi A, Wu X, Tokatli-Apollon A, El-Rifai M, Lee H, Zhang Y, et al. Amplifying the Red-Emission of Upconverting Nanoparticles for Biocompatible Clinically Used Prodrug-Induced Photodynamic Therapy. *ACS Nano*. 2014; 8: 10621-30.
- Kam NWS, O'Connell M, Wisdom JA, Dai HJ. Carbon nanotubes as multifunctional biological transporters and near-infrared agents for selective cancer cell destruction. *P Natl Acad Sci U S A*. 2005; 102: 11600-5.
- Qin W, Ding D, Liu J, Yuan WZ, Hu Y, Liu B, et al. Biocompatible Nanoparticles with Aggregation-Induced Emission Characteristics as Far-Red/Near-Infrared Fluorescent Bioprobes for In Vitro and In Vivo Imaging Applications. *Adv Funct Mater*. 2012; 22: 771-9.
- Li K, Zhu Z, Cai P, Liu R, Tomczak N, Ding D, et al. Organic Dots with Aggregation-Induced Emission (AIE Dots) Characteristics for Dual-Color Cell Tracing. *Chem Mater*. 2013; 25: 4181-7.
- Ding D, Li K, Liu B, Tang BZ. Bioprobes Based on AIE Fluorogens. *Accounts Chem Res*. 2013; 46: 2441-53.
- Hong Y, Lam JWY, Tang BZ. Aggregation-induced emission. *Chem Soc Rev*. 2011; 40: 5361-88.
- Hu QL, Gao M, Feng GX, Chen XD, Liu B. A Cell Apoptosis Probe Based on Fluorogen with Aggregation Induced Emission Characteristics. *ACS Appl Mater Interfaces*. 2015; 7: 4875-82.
- Li M, Gao Y, Yuan YY, Wu YZ, Song ZF, Tang BZ, et al. One-Step Formulation of Targeted Aggregation-Induced Emission Dots for Image-Guided Photodynamic Therapy of Cholangiocarcinoma. *ACS Nano*. 2017; 11: 3922-32.
- Ding D, Liang J, Shi HB, Kwok RTK, Gao M, Feng GX, et al. Light-up bioprobe with aggregation-induced emission characteristics for real-time apoptosis imaging in target cancer cells. *J Mater Chem B*. 2014; 2: 231-8.
- Yuan Y, Zhang C-J, Gao M, Zhang R, Tang BZ, Liu B. Specific Light-Up Bioprobe with Aggregation-Induced Emission and Activatable Photoactivity for the Targeted and Image-Guided Photodynamic Ablation of Cancer Cells. *Angew Chem Int Ed Engl*. 2015; 54: 1780-6.
- Ichikawa Y, Kamiya M, Obata F, Miura M, Terai T, Komatsu T, et al. Selective Ablation of β -Galactosidase-Expressing Cells with a Rationally Designed Activatable Photosensitizer. *Angew Chem Int Ed Engl*. 2014; 53: 6772-5.
- Yuan Y, Zhang C-J, Kwok RTK, Xu S, Zhang R, Wu J, et al. Light-Up Probe for Targeted and Activatable Photodynamic Therapy with Real-Time In Situ Reporting of Sensitizer Activation and Therapeutic Responses. *Adv Funct Mater*. 2015; 25: 6586-95.
- Liang J, Tang BZ, Liu B. Specific light-up bioprobes based on AIEgen conjugates. *Chem Soc Rev*. 2015; 44: 2798-811.
- Wu W, Mao D, Hu F, Xu S, Chen C, Zhang C-J, et al. A Highly Efficient and Photostable Photosensitizer with Near-Infrared Aggregation-Induced Emission for Image-Guided Photodynamic Anticancer Therapy. *Adv Mater*. 2017; 29: 1700548.
- Gu B, Wu W, Xu G, Feng G, Yin F, Chong PHJ, et al. Precise Two-Photon Photodynamic Therapy using an Efficient Photosensitizer with Aggregation-Induced Emission Characteristics. *Adv Mater*. 2017; 29: 1701076.
- Lin QN, Huang Q, Li CY, Bao CY, Liu ZZ, Li FY, et al. Anticancer Drug Release from a Mesoporous Silica Based Nanophotocage Regulated by Either a One- or Two-Photon Process. *J Am Chem Soc*. 2010; 132: 10645-7.
- Ogawa K, Kobuke Y. Recent advances in two-photon photodynamic therapy. *Anticancer Agents Med Chem*. 2008; 8: 269-79.
- Zhao LZ, Peng JJ, Huang Q, Li CY, Chen M, Sun Y, et al. Near-Infrared Photoregulated Drug Release in Living Tumor Tissue via Yolk-Shell Upconversion Nanocages. *Adv Funct Mater*. 2014; 24: 363-71.
- Chen G, Qiu H, Prasad PN, Chen X. Upconversion Nanoparticles: Design, Nanochemistry, and Applications in Theranostics. *Chem Rev*. 2014; 114: 5161-214.
- Liu XM, Fan ZQ, Zhang L, Jin Z, Yan DM, Zhang YL, et al. Bcl-2 inhibitor uploaded upconversion nanophotosensitizers to overcome the photodynamic therapy resistance of cancer through adjuvant intervention strategy. *Biomaterials*. 2017; 144: 73-83.
- Zhao H, Hu WB, Ma HH, Jiang RC, Tang YF, Ji Y, et al. Photo-Induced Charge-Variable Conjugated Polyelectrolyte Brushes Encapsulating Upconversion Nanoparticles for Promoted siRNA Release and Collaborative Photodynamic Therapy under NIR Light Irradiation. *Adv Funct Mater*. 2017; 27: 1702592.
- Lin M, Gao Y, Diefenbach TJ, Shen JK, Hornicek FJ, Park YI, et al. Facial Layer-by-Layer Engineering of Upconversion Nanoparticles for Gene Delivery: Near-Infrared-Initiated Fluorescence Resonance Energy Transfer Tracking and Overcoming Drug Resistance in Ovarian Cancer. *ACS Appl Mater Interfaces*. 2017; 9: 7941-9.
- Ma Y, Ji Y, You M, Wang S, Dong Y, Jin G, et al. Labeling and long-term tracking of bone marrow mesenchymal stem cells in vitro using NaYF₄:Yb(3+),Er(3+) upconversion nanoparticles. *Acta Biomaterialia*. 2016; 42: 199-208.
- Zhao B, Yin J-J, Bilski PJ, Chignell CF, Roberts JE, He Y-Y. Enhanced photodynamic efficacy towards melanoma cells by encapsulation of Pc4 in silica nanoparticles. *Toxicol Appl Pharmacol*. 2009; 241: 163-72.
- Xiao L, Gu L, Howell SB, Sailor MJ. Porous silicon nanoparticle photosensitizers for singlet oxygen and their phototoxicity against cancer cells. *ACS nano*. 2011; 5: 3651-9.
- Bernard AB, Lin C-C, Anseth KS. A Microwell Cell Culture Platform for the Aggregation of Pancreatic beta-Cells. *Tissue Eng Part C Methods*. 2012; 18: 583-92.
- Deng R, Qin F, Chen R, Huang W, Hong M, Liu X. Temporal full-colour tuning through non-steady-state upconversion. *Nat Nanotechnol*. 2015; 10: 237.

42. Feng W, Zhu X, Li F. Recent advances in the optimization and functionalization of upconversion nanomaterials for in vivo bioapplications. *NPG Asia Mater.* 2013; 5: e75.
43. You M, Lin M, Gong Y, Wang S, Li A, Ji L, et al. Household Fluorescent Lateral Flow Strip Platform for Sensitive and Quantitative Prognosis of Heart Failure Using Dual-Color Upconversion Nanoparticles. *ACS Nano.* 2017; 11: 6261-70.
44. You M, Zhong J, Hong Y, Duan Z, Lin M, Xu F. Inkjet printing of upconversion nanoparticles for anti-counterfeit applications. *Nanoscale.* 2015; 7: 4423-31.
45. Yang B, Zhang X, Zhang X, Huang Z, Wei Y, Tao L. Fabrication of aggregation-induced emission based fluorescent nanoparticles and their biological imaging application: recent progress and perspectives. *Mater Today.* 2016; 19: 284-91.
46. Kooijmans SAA, Fliervoet LAL, van der Meel R, Fens MHAM, Heijnen HFG, Henegouwen PMPvBE, et al. PEGylated and targeted extracellular vesicles display enhanced cell specificity and circulation time. *J Control Release.* 2016; 224: 77-85.
47. Feng L, Zhu C, Yuan H, Liu L, Lv F, Wang S. Conjugated polymer nanoparticles: preparation, properties, functionalization and biological applications. *Chem Soc Rev.* 2013; 42: 6620-33.
48. Zhang CJ, Hu QL, Feng GX, Zhang RY, Yuan YY, Lu XM, et al. Image-guided combination chemotherapy and photodynamic therapy using a mitochondria-targeted molecular probe with aggregation-induced emission characteristics. *Chem Sci.* 2015; 6: 4580-6.
49. Li K, Qin W, Ding D, Tomczak N, Geng J, Liu R, et al. Photostable fluorescent organic dots with aggregation-induced emission (AIE dots) for noninvasive long-term cell tracing. *Sci Rep.* 2013; 3: 1150.
50. Jin G, Feng C, Qin W, Tang BZ, Liu B, Li K. Multifunctional organic nanoparticles with aggregation-induced emission (AIE) characteristics for targeted photodynamic therapy and RNA interference therapy. *Chem Commun.* 2016; 52: 2752-5.
51. Yong K-T, Law W-C, Hu R, Ye L, Liu L, Swihart MT, et al. Nanotoxicity assessment of quantum dots: from cellular to primate studies. *Chem Soc Rev.* 2013; 42: 1236-50.
52. Su Y, Hu M, Fan C, He Y, Li Q, Li W, et al. The cytotoxicity of CdTe quantum dots and the relative contributions from released cadmium ions and nanoparticle properties. *Biomaterials.* 2010; 31: 4829-34.
53. Hadjuc C, Lange N, Rebstein J, Monnier P, van den Bergh H, Wagnieres G. Spectroscopic studies of photobleaching and photoproduct formation of meta(tetrahydroxyphenyl) chlorin (m-THPC) used in photodynamic therapy. The production of singlet oxygen by m-THPC. *J Photochem Photobiol B.* 1998; 45: 170-8.
54. Guan Y, Lu H, Li W, Zheng Y, Jiang Z, Zou J, et al. Near-Infrared Triggered Upconversion Polymeric Nanoparticles Based on Aggregation-Induced Emission and Mitochondria Targeting for Photodynamic Cancer Therapy. *ACS Appl Mater Interfaces.* 2017; 9: 26731-9.
55. Shah SB, Singh A. Cellular self-assembly and biomaterials-based organoid models of development and diseases. *Acta Biomater.* 2017; 53: 29-45.
56. Xiong L, Shuhendler AJ, Rao J. Self-luminescing BRET-FRET near-infrared dots for in vivo lymph-node mapping and tumour imaging. *Nat Commun.* 2012; 3: 1193.
57. Qian CG, Yu JC, Chen YL, Hu QY, Xiao XZ, Sun WJ, et al. Light-Activated Hypoxia-Responsive Nanocarriers for Enhanced Anticancer Therapy. *Adv Mater.* 2016; 28: 3313-20.
58. Tsoi KM, MacParland SA, Ma X-Z, Spetzler VN, Echeverri J, Ouyang B, et al. Mechanism of hard-nanomaterial clearance by the liver. *Nat Mater.* 2016; 15: 1212-21.
59. Liu T, Choi H, Zhou R, Chen IW. RES blockade: A strategy for boosting efficiency of nanoparticle drug. *Nano Today.* 2015; 10: 11-21.
60. Parodi A, Quattrocchi N, van de Ven AL, Chiappini C, Evangelopoulos M, Martinez JO, et al. Synthetic nanoparticles functionalized with biomimetic leukocyte membranes possess cell-like functions. *Nat Nanotechnol.* 2012; 8: 61.
61. Li J, Zhen X, Lyu Y, Jiang Y, Huang J, Pu K. Cell Membrane Coated Semiconducting Polymer Nanoparticles for Enhanced Multimodal Cancer Phototheranostics. *Acs Nano.* 2018; 12: 8520-30.
62. Xuan M, Shao J, Zhao J, Li Q, Dai L, Li J. Magnetic Mesoporous Silica Nanoparticles Cloaked by Red Blood Cell Membranes: Applications in Cancer Therapy. *Angew Chem Int Ed Engl.* 2018; 57: 6049-53.
63. Ai X, Ho CJH, Aw J, Attia ABE, Mu J, Wang Y, et al. In vivo covalent cross-linking of photon-converted rare-earth nanostructures for tumour localization and theranostics. *Nat Commun.* 2016; 7: 10432.
64. Deng K, Li C, Huang S, Xing B, Jin D, Zeng Q, et al. Recent Progress in Near Infrared Light Triggered Photodynamic Therapy. *Small.* 2017; 13: 1702299.
65. Yuan Y, Feng G, Qin W, Tang BZ, Liu B. Targeted and image-guided photodynamic cancer therapy based on organic nanoparticles with aggregation-induced emission characteristics. *Chem Commun.* 2014; 50: 8757-60.
66. Yuan Y, Kwok RTK, Tang BZ, Liu B. Smart Probe for Tracing Cancer Therapy: Selective Cancer Cell Detection, Image-Guided Ablation, and Prediction of Therapeutic Response In Situ. *Small.* 2015; 11: 4682-90.
67. Zheng Z, Zhang T, Liu H, Chen Y, Kwok RTK, Ma C, et al. Bright Near-Infrared Aggregation-Induced Emission Luminogens with Strong Two-Photon Absorption, Excellent Organelle Specificity, and Efficient Photodynamic Therapy Potential. *ACS Nano.* 2018; DOI: 10.1021/acsnano.8b03138.
68. Zhen S, Wang S, Li S, Luo W, Gao M, Ng LG, et al. Theranostics: Efficient Red/Near-Infrared Fluorophores Based on Benzo[1,2-b:4,5-b']dithiophene 1,1,5,5-Tetraoxide for Targeted Photodynamic Therapy and In Vivo Two-Photon Fluorescence Bioimaging. *Adv Funct Mater.* 2018; 28: 1870087.
69. Wu W, Feng G, Xu S, Liu B. A Photostable Far-Red/Near-Infrared Conjugated Polymer Photosensitizer with Aggregation-Induced Emission for Image-Guided Cancer Cell Ablation. *Macromolecules.* 2016; 49: 5017-25.
70. Gu XG, Kwok RTK, Lam JWY, Tang BZ. AIEgens for biological process monitoring and disease theranostics. *Biomaterials.* 2017; 146: 115-35.
71. Gao YT, Feng GX, Jiang T, Goh CC, Ng LG, Liu B, et al. Biocompatible Nanoparticles Based on Diketo-Pyrrolo-Pyrrole (DPP) with Aggregation-Induced Red/NIR Emission for In Vivo Two-Photon Fluorescence Imaging. *Adv Funct Mater.* 2015; 25: 2857-66.
72. Zhao Z, Su HF, Zhang PF, Cai YJ, Kwok RTK, Chen YC, et al. Polyyne bridged AIE luminogens with red emission: design, synthesis, properties and applications. *J Mater Chem B.* 2017; 5: 1650-7.
73. Zhao QL, Zhang S, Liu Y, Mei J, Chen SJ, Lu P, et al. Tetraphenylethyl-modified perylene bisimide: aggregation-induced red emission, electrochemical properties and ordered microstructures. *J Mater Chem.* 2012; 22: 7387-94.
74. Zhou Z, Song J, Nie L, Chen X. Reactive oxygen species generating systems meeting challenges of photodynamic cancer therapy. *Chem Soc Rev.* 2016; 45: 6597-626.
75. Park YI, Lee KT, Suh YD, Hyeon T. Upconverting nanoparticles: a versatile platform for wide-field two-photon microscopy and multi-modal in vivo imaging. *Chem Soc Rev.* 2015; 44: 1302-17.
76. Li F, Du Y, Liu J, Sun H, Wang J, Li R, et al. Responsive Assembly of Upconversion Nanoparticles for pH-Activated and Near-Infrared-Triggered Photodynamic Therapy of Deep Tumors. *Adv Mater.* 2018; 0: 1802808.
77. Xu J, Xu L, Wang C, Yang R, Zhuang Q, Han X, et al. Near-Infrared-Triggered Photodynamic Therapy with Multitasking Upconversion Nanoparticles in Combination with Checkpoint Blockade for Immunotherapy of Colorectal Cancer. *ACS Nano.* 2017; 11: 4463-74.
78. Zhang Y, Huang P, Wang D, Chen J, Liu W, Hu P, et al. Near-infrared-triggered antibacterial and antifungal photodynamic therapy based on lanthanide-doped upconversion nanoparticles. *Nanoscale.* 2018; DOI: 10.1039/C8NR01967C.
79. Yuan D, Tan MC, Riman RE, Chow GM. Comprehensive Study on the Size Effects of the Optical Properties of NaYF₄:Yb,Er Nanocrystals. *J Phys Chem C Nanomater Interfaces.* 2013; 117: 13297-304.
80. Zhao J, Lu Z, Yin Y, McRae C, Piper JA, Dawes JM, et al. Upconversion luminescence with tunable lifetime in NaYF₄:Yb,Er nanocrystals: role of nanocrystal size. *Nanoscale.* 2013; 5: 944-52.
81. Gnanasamandhan MK, Idris NM, Bansal A, Huang K, Zhang Y. Near-IR photoactivation using mesoporous silica-coated NaYF₄:Yb,Er/Tm upconversion nanoparticles. *Nat Protoc.* 2016; 11: 688-713.
82. Li XM, Wang R, Zhang F, Zhao DY. Engineering Homogeneous Doping in Single Nanoparticle To Enhance Upconversion Efficiency. *Nano Lett.* 2014; 14: 3634-9.
83. Chen GY, Shen J, Ohulchanskyy TY, Patel NJ, Kutikov A, Li ZP, et al. (alpha-NaYbF₄:Tm³⁺)/CaF₂ Core/Shell Nanoparticles with Efficient Near-Infrared to Near-Infrared Upconversion for High-Contrast Deep Tissue Bioimaging. *Acs Nano.* 2012; 6: 8280-7.
84. Chen G, Damasco J, Qiu H, Shao W, Ohulchanskyy TY, Valiev RR, et al. Energy-Cascaded Upconversion in an Organic Dye-Sensitized Core/Shell Fluoride Nanocrystal. *Nano Lett.* 2015; 15: 7400-7.
85. Brown JM, William WR. Exploiting tumour hypoxia in cancer treatment. *Nat Rev Cancer.* 2004; 4: 437-47.
86. Song G, Liang C, Yi X, Zhao Q, Cheng L, Yang K, et al. Perfluorocarbon-Loaded Hollow Bi₂Se₃ Nanoparticles for Timely Supply of Oxygen under Near-Infrared Light to Enhance the Radiotherapy of Cancer. *Adv Mater.* 2016; 28: 2716-23.
87. Cheng Y, Cheng H, Jiang C, Qiu X, Wang K, Huan W, et al. Perfluorocarbon nanoparticles enhance reactive oxygen levels and tumour growth inhibition in photodynamic therapy. *Nat Commun.* 2015; 6: 8785.
88. Wang X-Q, Gao F, Zhang X-Z. Initiator-Loaded Gold Nanocages as a Light-Induced Free-Radical Generator for Cancer Therapy. *Angew Chem Int Ed Engl.* 2017; 56: 9029-33.